Theoretical and Applied Climatology (2024) 155:2669–2688
https://doi.org/10.1007/s00704-023-04780-y

RESEARCH

Effect of global gravity wave activity on tropopause variation characteristics from multiple GNSS-RO observations

Mohamed Darrag[1,2] · Shuanggen Jin[1,3,4] · Aalaa Samy[5]

Received: 11 October 2023 / Accepted: 3 December 2023 / Published online: 14 December 2023

Abstract
The tropopause variation is very complex and affects climate change in the upper-troposphere lower-stratosphere (UTLS). In this study, the relationship and interaction between global gravity wave (GW) activities in terms of potential energy (Ep) over an altitude range from 5 km below the lapse-rate tropopause (LRT) to 10 km above the LRT and LRT characteristics are investigated using data from 12 global navigation satellite system radio occultation (GNSS-RO) missions from June 2001 to June 2022. The LRT height (LRT-H) and LRT temperature (LRT-T) display an increasing trend, while the LRT pressure (LRT-P) depicts a decreasing trend. In height Band 1, which corresponds to a height range from 5 km below LRT to LRT level, the GW Ep is maximum, with an upward trend of about 0.62 J/kg per decade. In addition, in height Band 2, which corresponds to a height range from LRT level to 5 km above LRT level, the GW Ep shows an increasing trend of about 0.18 J/kg per decade. In the case of height Band 3, which corresponds to a height range from 5 km above LRT level to 10 km above LRT level, the GW Ep is minimum with a downward trend of about − 0.17 J/kg per decade. The highest correlation coefficients among GW Ep and LRT parameters (H, T, and P) are at the height Band 2, at about − 0.52, 0.76, and 0.6 for LRT-H, LRT-T, and LRT-P, respectively. The results of the empirical orthogonal function (EOF) analysis of LRT parameters and GW activity at all height bands indicate that all the studied parameters have an increasing variability pattern. In addition, the leading mode of spatial variability of GW Ep at height Band 2 agrees with that of LRT-T and LRT-P and has an opposite sign in the case of LRT-H. The singular value decomposition (SVD) analysis results reveal that the leading temporal variability paired mode of Ep and all LRT parameters has a significant positive correlation, while the spatial one shows a strong coupling between the patterns of the combined Ep in height Band 2 and LRT parameters. Both global GW Ep and tropopause parameters have a clear seasonal variation. The results illustrate that the variations of LRT parameters are most closely related to the variations of GW Ep at height Band 2. Furthermore, the close effect of GW's activity on tropopause variation characteristics is clearly evident.

1 Introduction

The tropopause is a crucial atmospheric boundary that separates the turbulent, wet troposphere from the stable, dry stratosphere. It is receiving more attention in climate change research. Many studies have indicated that the tropopause is rising as a result of global warming caused by increased greenhouse gas (GHG) emissions in the atmosphere (Meng et al. 2021; Pisoft et al. 2021; Darrag et al. 2022). The changes in tropopause characteristics can be considered a sensitive indicator of anthropogenic climate change in the upper-troposphere lower-stratosphere (UTLS) (Sausen and Santer 2003; Santer et al. 2004). The variations of tropopause parameters (height, temperature, and pressure) are closely related to atmospheric waves (Randel et al. 2003; Satheesan and Krishna Murthy 2005; Corrigan et al. 2006),

✉ Shuanggen Jin
sgjin@shao.ac.cn

1 School of Remote Sensing and Geomatics Engineering, Nanjing University of Information Science and Technology, Nanjing 210044, China

2 Geodynamic Department, National Research Institute of Astronomy and Geophysics-NRIAG, 11421 Helwan, Cairo, Egypt

3 School of Surveying and Land Information Engineering, Henan Polytechnic University, Jiaozuo 454003, China

4 Shanghai Astronomical Observatory, Chinese Academy of Sciences, Shanghai 200030, China

5 Geomagnetic and Geoelectric Department, National Research Institute of Astronomy and Geophysics-NRIAG, 11421 Helwan, Cairo, Egypt

among which the impact of gravity waves (GWs) is significant (Randel et al. 2003; Khan and Jin 2016). GWs play a crucial role in atmospheric circulation. It is one of the main drivers of atmospheric dynamics. GWs are mainly generated in the troposphere and then propagate upward transferring energy, momentum, water vapor, and chemical components between different atmosphere layers (Yang et al. 2021), which influence tropopause parameters directly or indirectly (Khan and Jin 2016). Understanding the sources and propagation of GWs is essential to improving weather and climate models (Perrett et al. 2021). Deep convection, winds gusting over mountains, jet streams, breaking of tidal and planetary waves, explosions, and instabilities at all heights are the primary GW sources (Fritts and Nastrom 1992; Fritts and Alexander 2003).

Several studies have examined the variability of the global tropopause structure (Schmidt et al. 2004; Seidel and Randel 2006; Li et al. 2017) and global GW activity (Tsuda et al. 2000; Wang and Alexander 2010), but there have been few studies on the relationship between GWs and the tropopause parameters on a global scale. The majority of studies focus on their interaction on a regional or local scale. Randel et al. (2003) used Global Positioning System Meteorology (GPS/MET) RO observations from April 1995 to February 1997 to examine the structure and variability of temperature in the tropical UTLS. They reported that GWs appeared to be responsible for much of the subseasonal variability in cold point tropopause (CPT) height and temperature. Using temperature data from the Constellation Observing System for Meteorology, Ionosphere, and Climate (COSMIC) Radio Occultation (RO), Khan and Jin (2016) investigated the effects of stratospheric GW activity on CPT parameters and water vapor over Tibet during June 2006 to February 2014. Their findings show how GWs affect stratospheric water vapor concentration and CPT temperature. Above the cold points, there is a strong correlation between water vapor, CPT temperature, and GW activity. Furthermore, Yu et al. (2019) investigated the relation between stratospheric GW Ep and tropopause parameters worldwide using dry temperature profiles from the COSMIC RO mission for the period September 2006 to May 2013. They found that stratospheric GW Ep has a significant positive correlation with lapse-rate tropopause (LRT) height (LRT-H) and a significant negative correlation with LRT temperature (LRT-T) in the stratosphere, with distinct zonal distribution characteristics at middle and high latitudes. They reported that it is possible to conclude that GW activities influence the variations of tropopause parameters. When GWs propagate from the troposphere to the stratosphere, the tropopause lifts and becomes cooler at middle and high latitudes, whereas in the tropics, both deep convections and GWs have an impact on the tropopause structure. According to Ayorinde et al. (2022), based on global navigation satellite systems radio occultation (GNSS-RO) data during 2020 and 2021, changes in the tropopause's characteristics are influenced by stratospheric GW activity. Deep convections and stratospheric GWs both had an impact on the tropopause's structure in the tropics, while at higher latitudes, the height of the tropopause showed more fluctuation as GWs moved from the troposphere to the stratosphere. Numerous studies have suggested that the tropopause region is a significant GW generating zone (Zhang et al. 2010, 2012). Furthermore, several studies on active GW motions in the tropopause region and their potential connections with local turbulence and mixing have been published (Sharman et al. 2012; Mchugh and Sharman 2013). Applying general circulation models (GCMs) and reanalysis data, Birner et al. (2006) proposed that the tropopause inversion layer (TIL) could have an effect on gravity wave propagation. On the other hand, using a high-resolution GCM to investigate the transport mechanism of GWs through the tropopause, Miyazaki et al. (2010) found that GW may have possible effects on the TIL. Kunkel et al. (2014) investigated the connection between inertial GWs (IGWs) and TIL based on simulation. They discovered that the thermal and dynamical structures of the tropopause region may be persistently changed by the energy dissipation, local heating, and turbulence caused by IGWs; these processes may lead to the production of TIL or alter an existing one.

The study of global GWs' influence on tropopause characteristics is a difficult task due to data limitations and the complexity of the Earth's atmospheric system. The limitations of the used techniques are the low spatial resolution of the radiosonde (RS) observations, which mainly cover land and show sparse data in the ocean and polar regions. Moreover, it displays an asymmetrical distribution in both hemispheres. For the satellite remote sensing technologies and model analyses, both suffer from coarse vertical resolution. In addition, the reanalysis data trends can be biased to reflect changes in both the quantity and quality of the underlying data (Schmidt et al. 2004; Li et al. 2017). GNSS-RO has provided an exceptional technique to retrieve land surface and atmospheric parameters globally (Jin 2012; Jin et al. 2011, 2019, 2014, 2017). The GNSS-RO technique was first performed within the GPS/MET experiment for the period 1995 to 1997 (Kursinski et al. 1997). Then, it has been continuously applied aboard various low-Earth orbit (LEO) satellite missions since 2001. By 2025, the planned missions will provide a global coverage of about 14,700 RO profiles daily (Jin et al. 2014; Oscar 2023). The GNSS-RO technique has many advantages, such as uniform global coverage, a higher vertical resolution than any of the existing satellite temperature measurements available for the UTLS, long-term stability, and the ability to work in all weather conditions unaffected by clouds, precipitation, or aerosols (Bai et al. 2020; Scherllin-Pirscher et al. 2021). GNSS-RO

neutral atmospheric measurements are performed for the height range from the lowest troposphere to ~ 80 km. The highest quality of GNSS-RO atmospheric profiles is at altitudes between ~ 8 and ~ 35 km; thus, it is well suited for the climatology of the UTLS (Kursinski et al. 1997; Foelsche et al. 2008; Zeng et al. 2019). The accuracy of RO data in the UTLS typical estimates is ~ 0.1 K from 8 to 30 km (Ho et al. 2020; Tegtmeier et al. 2020). The GNSS-RO technique enables measuring the thermal structure of the atmosphere with a vertical resolution of 100 m near the surface to 1.5 km at 40 km (Kumar et al. 2014; Ho et al. 2012). Although there are many advantages to GNSS-RO observations in UTLS, the application of GNSS-RO measurement in the lower troposphere is a challenging task due to the biases of GNSS-RO observations in the lower troposphere that are caused by multi-path and high refractivity gradients (Beyerle et al. 2006; Cucurull 2010). GNSS-RO measurements are well suited for studying tropopause characteristics (Xu et al. 2014) and global GW activity (Wang and Alexander 2010; Schmidt et al. 2016). Many studies have confirmed the feasibility and excellent suitability of GNSS-RO measurements for atmospheric monitoring and climate change detection (Steiner et al. 2011).

In this study, we aim to investigate the relation between the global GW activity in terms of potential energy (Ep) and the LRT parameters for the first time using data from 12 GNSS-RO missions from June 2001 to June 2022. In Section 2, the GNSS-RO data used in our study are depicted. In addition, the methods to derive the global tropopause and GW parameters are presented. Moreover, the data analysis is explained. Section 3 describes and discusses the results and findings. Finally, conclusion and summary are given in Section 4.

2 Data and methods

2.1 Data

In the investigation of the relationship between global GW activity and tropopause characteristics, we use GNSS-RO atmospheric profile data from 12 LEO satellite missions for the period from June 2001 to June 2022, which are combined together to provide good spatial and temporal coverage worldwide. In this study, the utilized atmospheric retrievals are level 2 dry temperature profiles that are freely available at the University Corporation for Atmospheric Research (UCAR), COSMIC Data Analysis and Archive Center (CDAAC). The availability of the used GNSS-RO data and its temporal span is depicted in Fig. 1 (CDAAC 2022).

2.2 Methods

The used GNSS-RO atmospheric profile data from various LEO missions is highly consistent (Darrag et al. 2022). All the utilized dry temperature profiles are first spline interpolated to a regular 100 m height resolution to determine the tropopause and GW parameters globally (Hindley et al. 2015). The tropopause parameters are determined by applying the LRT definition. According to the World Meteorological Organization (WMO) tropopause definition, "The thermal LRT is defined as the lowest level at which the lapse rate decreases to 2 °C/km or less, provided also the average lapse rate between this level and all higher levels within 2 km does not exceed 2 °C/km" (WMO 1957). The GW Ep is independently estimated from each temperature profile over an altitude range from 5 km below the LRT (LRT-5 km) to

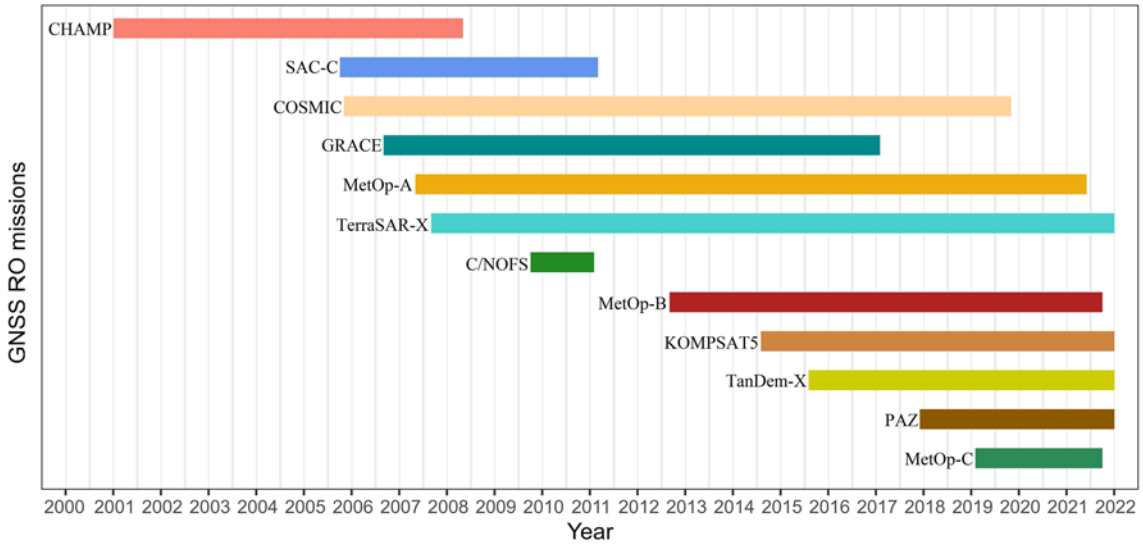

Fig. 1 Available global navigation satellite systems radio occultation (GNSS-RO) data used in this study

10 km above the LRT (LRT + 10 km). The raw temperature profile $T(z)$ can be separated into background temperature $\overline{T}(z)$ and temperature fluctuation $T'(z)$ by applying the GWs linear theory (Fritts and Alexander 2003). The separation of the temperature profile into background $\overline{T}(z)$ and a fluctuation $T'(z)$ is performed following the method of Alexander et al. (2011) that reduces artificial enhancements around the tropopause through applying double filtering steps, the first of which is bandpass filtering of the temperature profile $T(z)$ using a cutoff of 2–10 km which is the wavelength of interest in our study, and the second step is low-pass filtering of the temperature fluctuation component using a 10 km cutoff to minimize the effect of the high temperature gradient at the tropopause on the calculated Ep values.

$$T'(z) = T(z) - \overline{T}(z) \tag{1}$$

The Brunt–Väisälä frequency squared $N^2(z)$ profile is computed applying the following equation:

$$N^2 = \frac{g}{T}\left(\frac{\partial \overline{T}}{\partial z} + \frac{g}{c_p}\right)^2 \tag{2}$$

where g denotes gravity acceleration and c_p denotes air-specific heat capacity at constant pressure.

The Ep profile is computed by Eq. 3:

$$E_P = \frac{1}{2}\left(\frac{g}{N}\right)^2 \bullet \left(\frac{T'}{\overline{T}}\right)^2 \tag{3}$$

The Ep profile over the studied height range is divided into three height bands. Band 1 corresponds to a height range from 5 km below LRT to LRT level (LRT-5 km); Band 2 corresponds to a height range from LRT level to 5 km above LRT level (LRT + 5 km); Band 3 corresponds to a height range from 5 km above LRT level to 10 km above LRT level (LRT + 5 to LRT + 10 km). For each profile, the Ep of each height band is averaged. The results of all tropopause parameters and GW Ep bands are then grided into a $5° \times 5°$ latitude and longitude grid (Alexander et al. 2011; Khan and Jin 2016; Yu et al. 2019). The relation between tropopause parameters and GW Ep parameters is deeply examined and discussed. Furthermore, the spatial and temporal variability of the studied parameters is widely investigated using the empirical orthogonal function (EOF) technique, also known as the principal component analysis (PCA) (Bjornsson and Venegas 1997; Calabia and Jin 2020). This technique is commonly applied for climate variables' spatial and temporal analysis. It provides the spatial patterns of variability and expansion coefficient time series for a single geophysical variable in addition to the contribution of each mode of variability to the total variance. Because the variability of the studied parameters is mostly driven by the annual variation, the first PCA component is the only one considered for each variable. Wavelet coherence (WTC) analysis is performed to clarify the relation between the leading mode (PC1) of temporal variability of GW Ep at all height bands and that of LRT parameters. Within the time–frequency space, WTC can be utilized to estimate the coherence between two time series data that range between 0 and 1 (Grinsted et al. 2004). For further examination, we apply singular value decomposition (SVD) analysis to reveal the coupled modes of covariability between GW activity and LRT parameters. Before applying EOF and SVD analyses, the linear trends and seasonal cycles of each variable are removed to obtain the fields of anomalies. The SVD method can identify the pairs of coupled spatial modes and their temporal variation; it also provides the percentage of covariance fraction explained by each pair (Bjornsson and Venegas 1997; Dubache et al. 2019). In addition, the seasonal variation of global GW Ep and LRT parameters is widely examined.

3 Results and discussion

3.1 Relation between GW Ep and LRT parameters

It is clear in Fig. 2 that GW activity, represented by Ep, is at its maximum in height Band 1 (LRT-5 km) (Fig. 2a). The Ep decreases gradually upward to be the minimum in the height Band 3 (LRT + 5 to LRT + 10 km) (Fig. 2c), showing agreement with the results reported by Schmidt et al. (2008). The atmospheric GW activity is high in altitude Band 1 because most GWs are generated in the troposphere and propagate vertically until they become weak, at which point they dissipate, releasing energy and momentum into the general circulation (Zhang et al. 2015; Khan and Jin 2016). GW Ep in height Band 1 (Fig. 2a) shows the maximum increasing trend of 0.62 J/kg per decade, and GW Ep in height Band 2 (Fig. 2b) depicts an upward trend of 0.18 J/kg per decade. GW Ep in height Band 3 (Fig. 2c) exhibits a downward trend of − 0.17 J/kg per decade (Table 1).

Figure 3 shows the global LRT parameters from June 2001 to June 2022. Our analysis results signify a global increase in LRT-H of 30 m/decade since June 2001 (Fig. 3a), and this is in good agreement with that of Schmidt et al. (2008), which showed an upward trend in global LRT-H of 39–66 m/decade. In addition, the LRT-T has an upward trend of 0.13 k/decade (Fig. 3b), but the LRT-P has a downward trend of − 0.76 hPa/decade (Fig. 3c). The tropopause trends from our analysis are in agreement with those from previous studies (Sausen and Santer 2003; Schmidt et al. 2004; Seidel and Randel 2006; Meng et al. 2021). As shown in Fig. 4, the highest correlation coefficient between GW Ep and LRT parameters is about 0.76 between Ep in Band 2 and LRT-T. LRT-H has a positive correlation with GW Ep in height Band 1 (tropospheric) of 0.12, while it has a negative

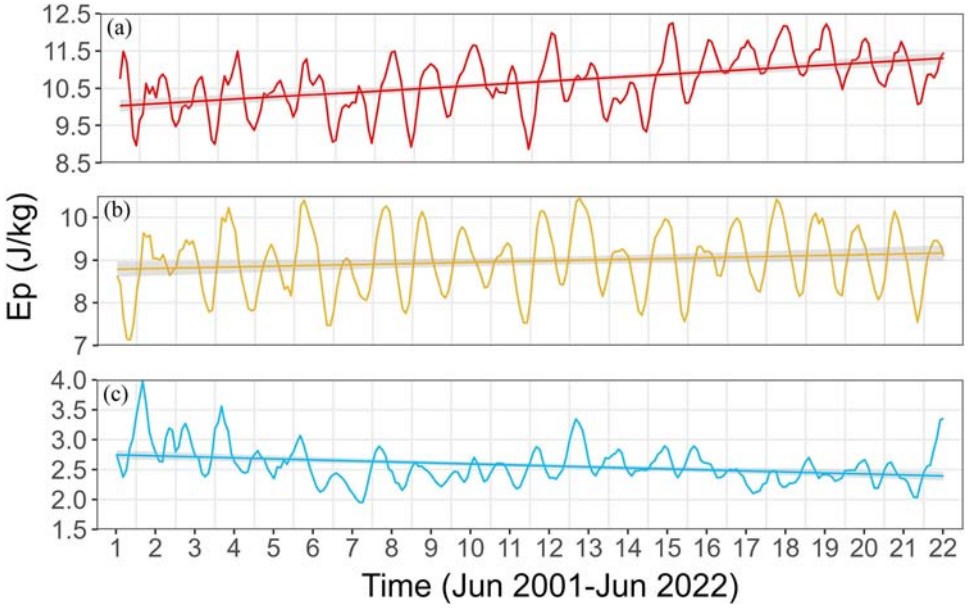

Fig. 2 Monthly time series of globally averaged GW Ep are represented in 3 height bands: **a** GW Ep averaged over the 5 km under LRT, **b** GW Ep averaged over the 5 km above LRT, and **c** GW Ep averaged over the altitude range from LRT + 5 km to LRT + 10 km for the period June 2001 to June 2022

Table 1 The global GW Ep, maximum, minimum, and standard deviation (SD) over an altitude range from 5 km under LRT to 10 km above LRT divided into 3 height bands of 5 km each, for the period June 2001 to June 2022. In addition to global Ep trends with a 95% confidence interval for all levels

Height level	Min Ep (J/kg)	Max Ep (J/kg)	Ep SD	Ep trend (J/kg) per decade
Band 1 (LRT-5 km)	8.86	12.25	0.74	0.62 ± 0.02
Band 2 (LRT + 5 km)	7.12	10.45	0.75	0.18 ± 0.02
Band 3 (LRT + 5 to LRT + 10 km)	1.95	3.97	0.31	− 0.17 ± 0.02

correlation of − 0.52 and − 0.49 with GW Ep in height Bands 2 and 3 (stratospheric), respectively. For LRT-T, it has a positive correlation with GW Ep at all height bands. In contrast to LRT-H, LRT-P has a negative correlation with GW Ep in height Band 1, while it has a positive correlation with GW Ep in height Bands 2 and 3. In addition, LRT-H has a correlation of − 0.75 and − 0.98 with LRT-T and LRT-P, respectively. GW Ep in Band 1 has a correlation of 0.63 and − 0.12 with that of Band 2 and Band 3, respectively. Meanwhile, GW Ep in Band 2 has a correlation of 0.35 with that of Band 3.

3.2 Spatial–temporal variability of GW Ep and LRT parameters

For the EOF analysis results of GW Ep and LRT parameters, we only consider the first leading mode, which explains the majority of the spatial structures and temporal variability. The first dominant pattern of spatial variability is represented as EOF1, while that of temporal variability is represented as PC1. The amplitudes of all EOF modes are normalized by multiplying each EOF by the SD of the corresponding temporal components. Therefore, each spatial pattern is considered an anomaly map with the same units as the original data (Forootan et al. 2012). In the case of LRT parameters (Fig. 5b, d, f), the EOF1 of LRT-H explains about 25.56% of the total variability, with values between − 1.36 and 2.06 km. For LRT-T, EOF1 represents 36.25% of the total variance, with values ranging between − 10.1 and 5.36 k. The EOF1 of LRT-P accounts for 30.03% of the total variability, with values between − 65.7 and 40.2 hPa. The PC1 of all LRT parameters (Fig. 5a, c, e) shows increasing trends over the course of the study. Moreover, the PC1 of all LRT parameters is dominated by inter-annual oscillations. EOF1 of LRT-H shows two clear variability patterns, with different signs, at the transition zone from the tropics to the subtropics. The LRT-H positive variability pattern in northern hemisphere (NH) is stronger than the negative one in southern hemisphere (SH) (Fig. 5b). Due to the expansion of the tropics poleward, the LRT-H in NH exhibits rising patterns in the tropical edge latitude (TEL) region, which is the transitional zone from the tropics to the extratropics (Darrag et al. 2022). Furthermore, the LRT-H exhibits an increasing pattern in the polar regions of both hemispheres as a result of the high level of climate variability brought on by the rapid rise in surface temperature. For LRT-P

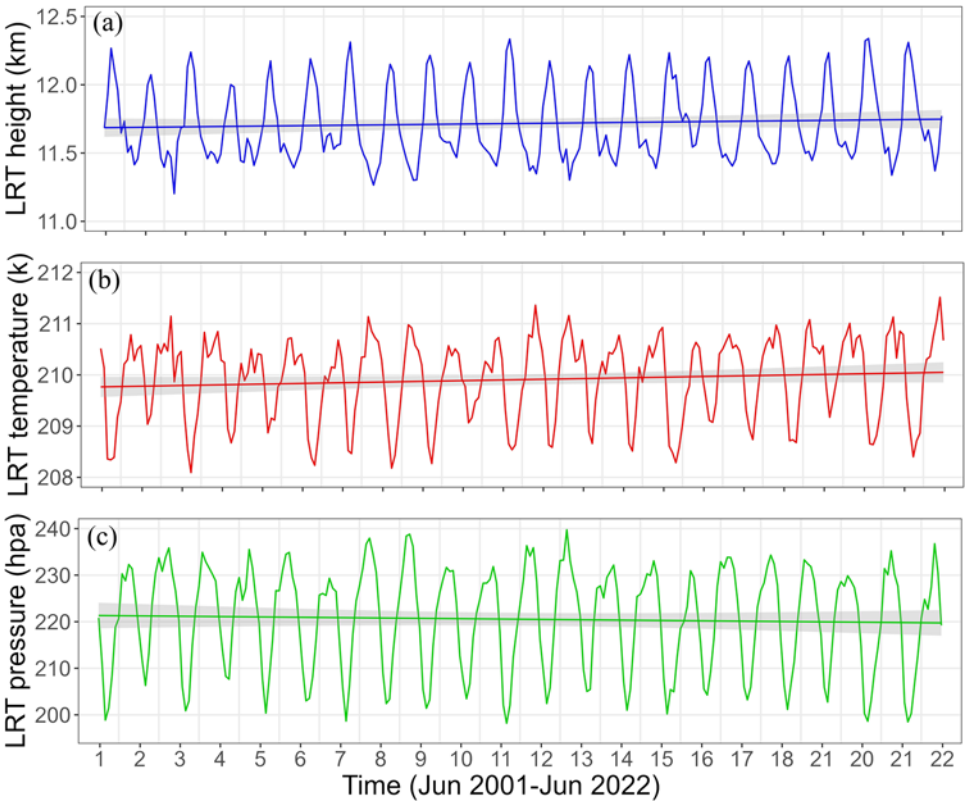

Fig. 3 Monthly time series of globally averaged LRT parameters (height, temperature, and pressure) for the period June 2001 to June 2022: **a** tropopause height, **b** tropopause temperature, and **c** tropopause pressure

EOF1 (Fig. 5f), it shows patterns of variability at the same locations as LRT-H but with different signs. In the case of LRT-T EOF1 (Fig. 5d), its spatial variability pattern agrees with that of LRT-P except that in the north pole, LRT-T displays a clear positive variability pattern that is weaker but wider than the negative one in the south pole. In addition, all LRT parameters show evident longitudinal variation in their spatial pattern in NH, mainly at the transition zone from the tropics to the subtropics. In contrast, the spatial pattern in SH shows slight longitudinal variation, which is not significant. Our results are in good agreement with those of Liu et al. (2014). The decreasing trends of tropopause parameters in the SH is largely due to the stratospheric polar vortex, which is colder in the SH than in the NH (Zängl and Hoinka 2001).

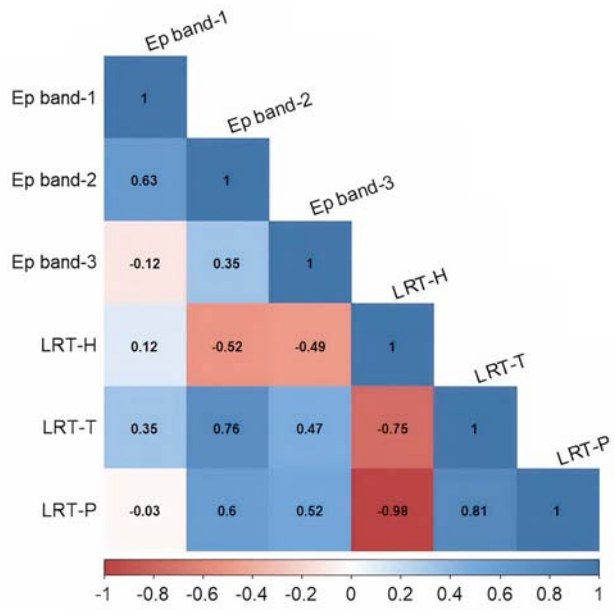

Fig. 4 The correlation coefficients among the monthly averaged LRT parameters and GW Ep at all levels over an altitude range from 5 km under LRT to 10 km above LRT, for the period June 2001 to June 2022

Figure 6 shows the EOF analysis results of GW Ep at different altitude bands. The main variability mode, EOF1, of Ep at height Band 1 accounts for 6.91% of the total data variance, with values between − 2.5 and 3.74 J/kg (Fig. 6b). In the case of height Band 2, EOF1 of GW Ep describes 12.37% of the total variability, with values ranging between − 4.6 and 3.2 J/kg (Fig. 6d). The EOF1 of Ep at height Band 3 explains 4.98% of the total data variance, with values between − 2.6 and 0.4 J/kg (Fig. 6f). The PC1 of Ep at all height levels (Fig. 6a, c, e) has shown increasing trends throughout the study period. Furthermore, the PC1 of GW Ep at height Bands 1 and 2 is dominated by inter-annual oscillations. Ep EOF1 in altitude Band 1 shows two variability patterns with different signs around the equator (Fig. 6b).

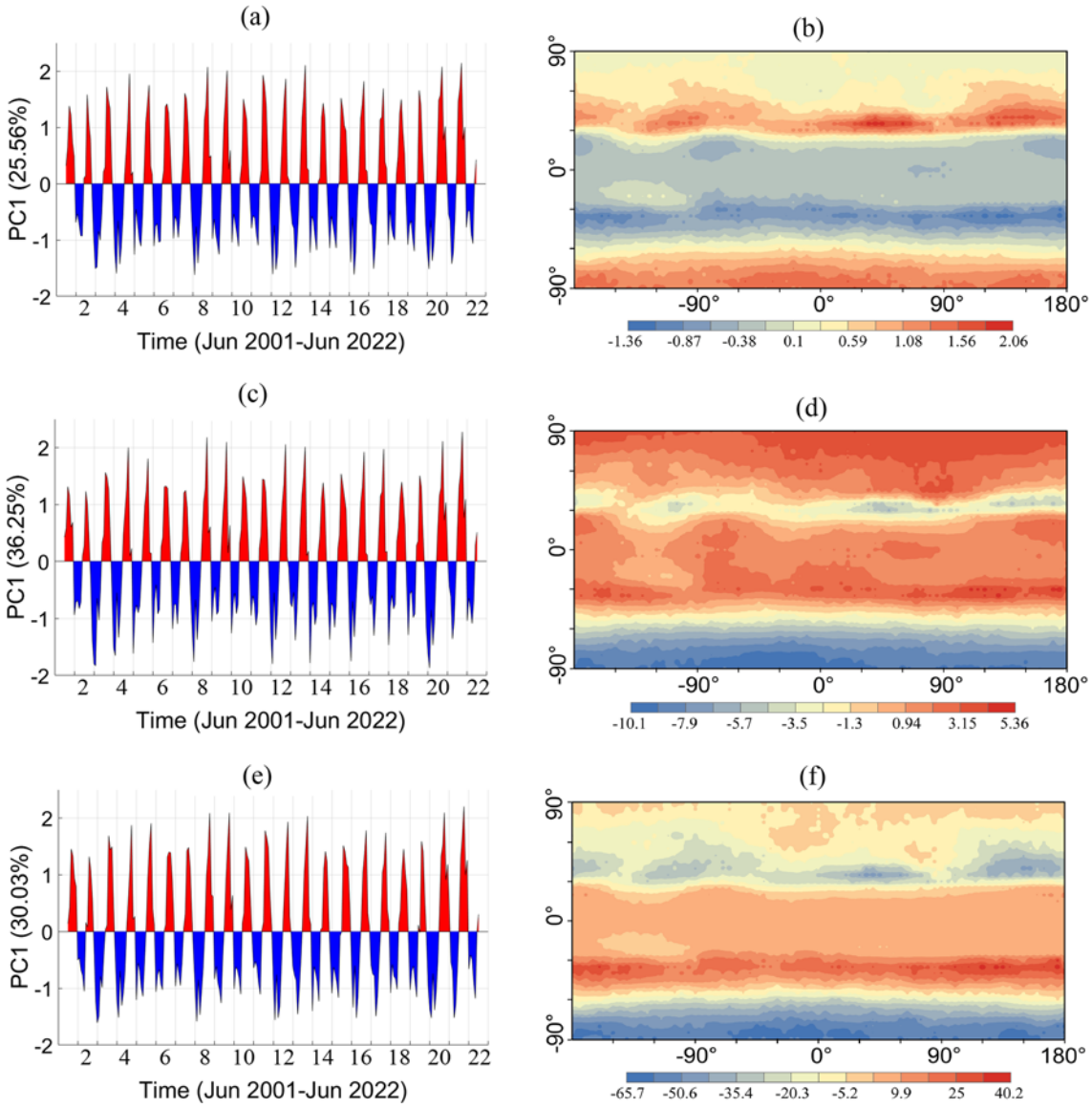

Fig. 5 LRT parameters first leading mode of variability, LRT-H (**a**, **b**), LRT-T (**c**, **d**), and LRT-P (**e**, **f**). The temporal variability time series given by PC1 (left) and the spatial map of variability given by EOF1 (right)

In addition, there are two wide patterns of spatial variability, with opposite signs, in the polar zones of both hemispheres. The spatial occurrence of variability patterns in Ep Band 1 matches that of all LRT parameters, but with the opposite signs in the case of LRT-H. The variability of GW activity below the tropopause in NH is linked to the subtropical and polar jet streams (Namboothiri et al. 2008). In the case of Ep Band 2 (Fig. 6d), the main mode of spatial variability, EOF1, shows an obvious pattern that looks like that of Ep Band 1 but is clearer. As in Band 2, the two variability patterns around the tropical zone show clear variability signals with less interference with those at the tropics. In addition, in Band 2, the Ep variability at the south pole is stronger than that in Band 1. The EOF1 mode of Ep Band 2 clearly matches that of the LRT parameters, but with the opposite signs in the case of LRT-H. The Ep in Band 1 and Band 2 has upward tends over the tropics because of convection that is considered a primary source of GW activity (Ratnam et al. 2004). For Ep Band 3 (Fig. 6f), EOF1 is characterized by a strong negative variability mode around the equator. In addition, a weak positive variability pattern covers the whole spatial domain from the equatorial zone poleward in both hemispheres. The EOF1 mode of Ep in Band 3 has no agreement with that of any LRT parameter. Our findings are consistent with those of Namboothiri et al. (2008), who used GPS-RO data from the Champ RO mission for the years 2001–2005 to explore the worldwide GW Ep variation in the troposphere and stratosphere. Figure 7 exhibits

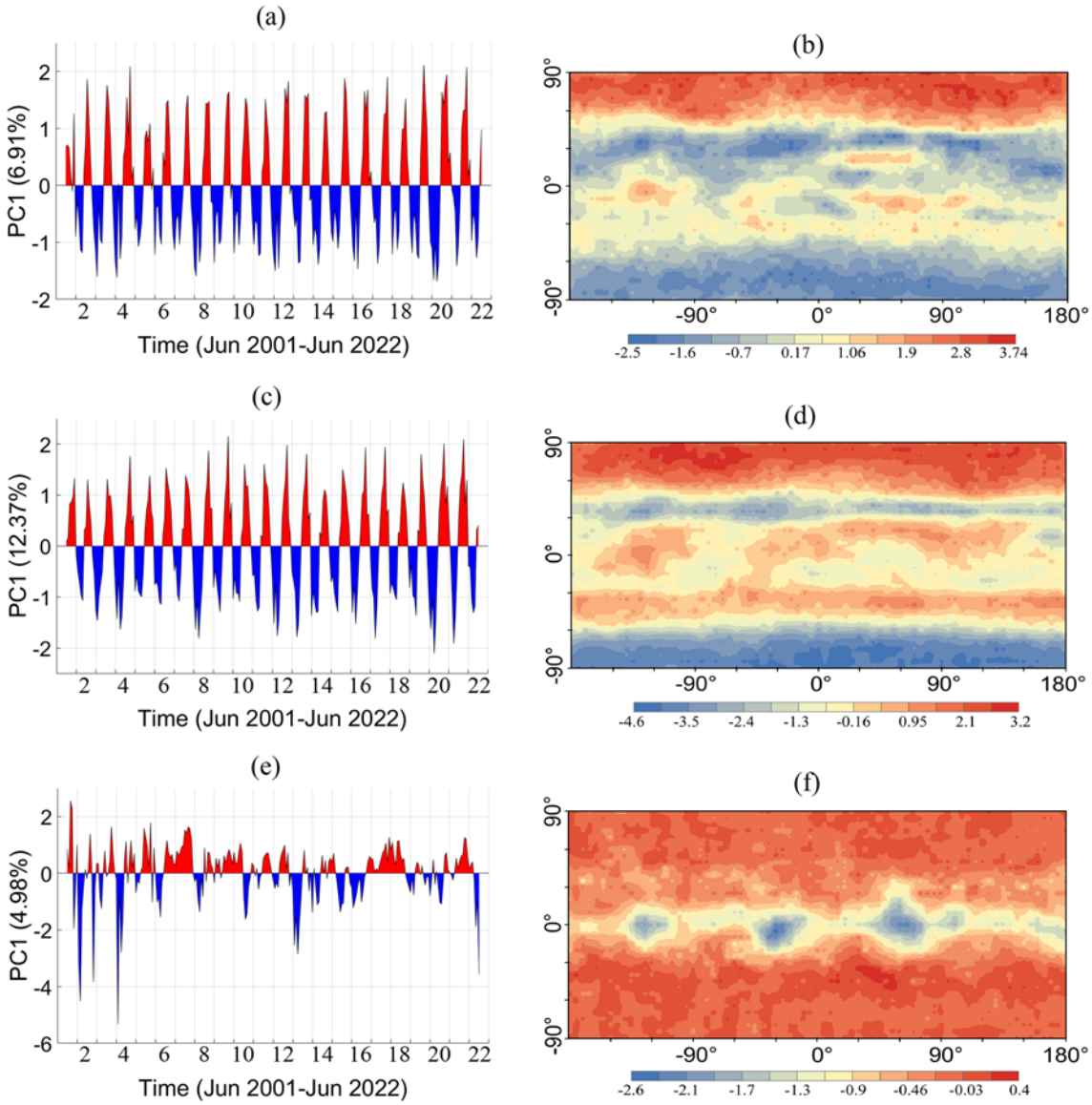

Fig. 6 The first leading mode of variability for the global GW Ep is at height Band 1, which corresponds to a height range from 5 km below LRT to LRT level (**a**, **b**), height Band 2, which corresponds to a height range from LRT level to 5 km above LRT level (**c**, **d**), and height Band 3, which corresponds to a height range from 5 km above LRT level to 10 km above LRT level (**e**, **f**). The temporal variability time series provided by PC1 (left) and the spatial map of variability provided by EOF1 (right)

the results of the WTC analysis between the leading mode (PC1) of temporal variability of GW Ep at all height bands and that of LRT parameters. As is clear, at all height bands, the GW Ep and LRT parameters are in phase. GW activity at Band 1 and Band 2 has a high level of correlation with LRT parameters at different time scales along the study period. LRT-T has the highest coherence with GW Ep, especially at height Band 2. At the lower stratosphere (Band 2), the GW Ep and LRT parameters are more correlated. In the case of height Band 3, no significant coherence is observed between Ep and LRT parameters except at the scale of 8–16 months over the period from 2001 to 2007.

For further investigation into the effect of GW activity on LRT characteristics, the SVD analysis is performed to reveal the coupled patterns of covariability between GW Ep and LRT parameters. In terms of understanding the interactions between two fields, SVD outperforms EOF (Bretherton et al. 1992). For the SVD analysis results, the first dominant mode of covariability is the only one taken into account. SVD1 represents spatial patterns for the first paired mode of covariability, while SC1 represents the corresponding time series of the expansion coefficients for the paired mode. For all used parameters in the SVD analysis, their SC1 timeseries and the corresponding SVD1 maps of spatial variability are

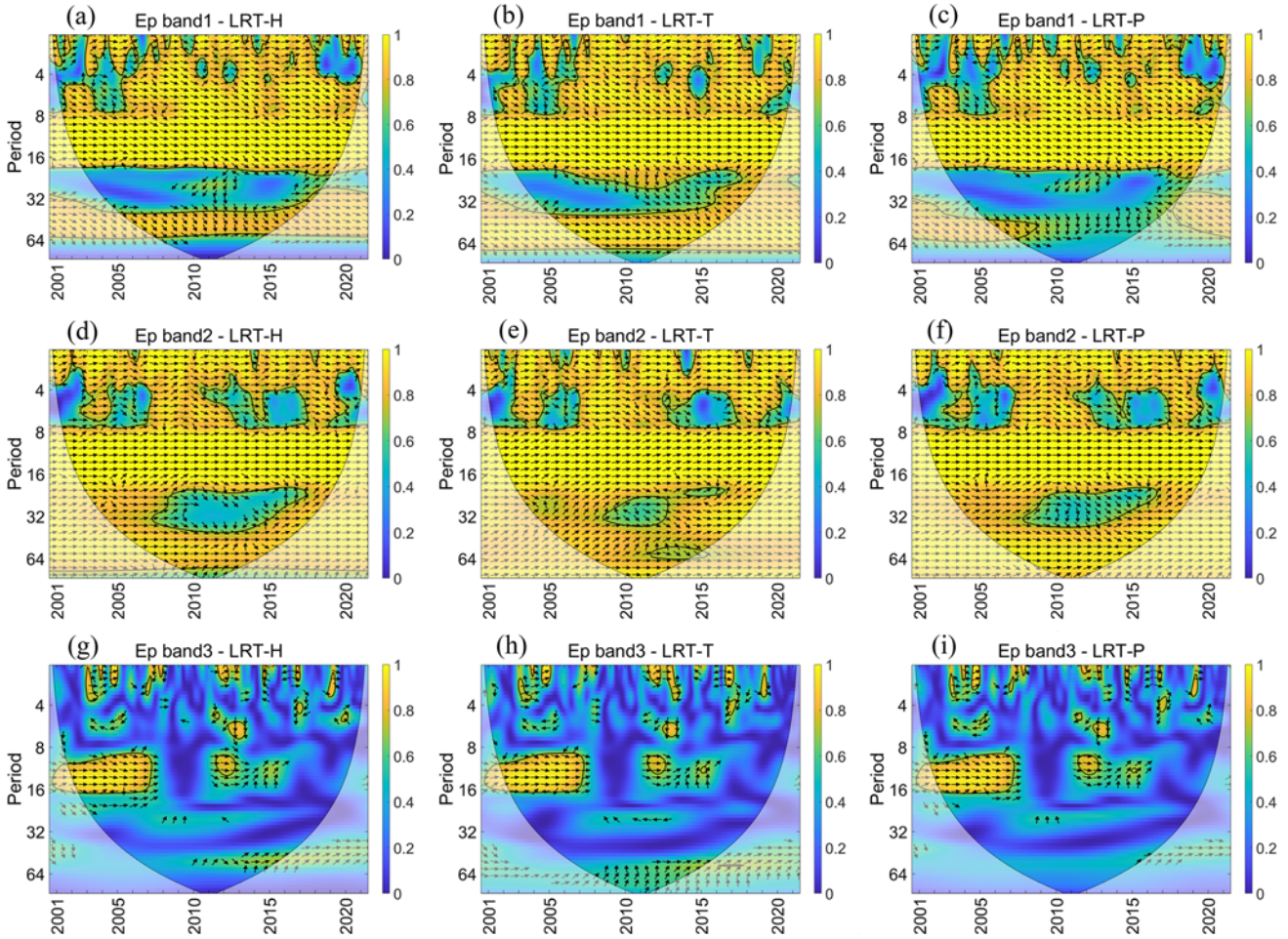

Fig. 7 Wavelet coherence (WTC) analysis between PC1 of GW Ep at all height bands and LRT parameters (LRT-H, LRT-T, and LRT-P). The phase differences between the two series are indicated by arrows. The variables are in phase when the arrows point to the right (they move in the same direction and have cyclical effects on each other). If the arrows point to the right and up, the first index is leading (it causes the second index). The first index is lagging if the arrows point down. The variables are out of phase (have anticyclical effects on each other) if the arrows point to the left. If the arrows point to the left and up, the first index is leading, and if they point to the left and down, the first index is lagging. Ep Band 1 on the top (**a**, **b**, **c**), Ep Band 2 on the middle (**d**, **e**, **f**), and Ep Band 3 on the bottom (**g**, **h**, **i**). LRT-H on the left (**a**, **d**, **g**), LRT-T on the middle (**b**, **e**, **h**), and LRT-P on the right (**c**, **f**, **i**)

scaled to span a range of [− 1 1] to facilitate the comparison and description of the paired modes of covariability.

The squared covariance fraction (SCF) of the first dominant mode for the coupled fields of GW Ep in height Band 1 against LRT-H, LRT-T, and LRT-P describes about 83.62%, 88.65%, and 86.27%, respectively, of the total covariability of both fields (Fig. 8). As is clear, SC1 of Ep Band 1 has a strong positive correlation with that of LRT-H, LRT-T, and LRT-P of 0.96, 0.97, and 0.95, respectively (Fig. 8c, f, i). Moreover, the SC1 for the temporal variability paired mode of Ep in height Band 1 and all LRT parameters is dominated by inter-annual oscillations. The first coupled mode of spatial variability, SVD1, demonstrates that the GW Ep in Band 1 (Fig. 8a) is characterized by observed fluctuations bands at the transitional zones from tropics to extratropics and in the two poles, at both hemispheres, accompanied by LRT-H (Fig. 8b) fluctuations of the opposite sign over the same regions. The first spatial variability paired mode of GW Ep in height Band 1 (Fig. 8d) and LRT-T (Fig. 8e), SVD1, shows that the GW Ep in Band 1 is characterized by observed fluctuation bands of opposite signs around the tropics and in the two poles, which are accompanied by LRT-T narrower fluctuations of the same sign over the same regions. In the case of SVD1 for the spatial variability paired mode of Ep in height Band 1 (Fig. 8g) and LRT-P (Fig. 8h), both have observed fluctuation bands that show good consistency around the tropics and in the two poles. Around the equator, GW Ep shows interfered positive and negative anomalies areas (Fig. 8a, d, g), but LRT-H depicts an area of positive anomalies (Fig. 8b). In the case of LRT-T and LRT-P (Fig. 8e, h), both exhibit areas of negative anomaly around the equator. The SVD analysis results show that the

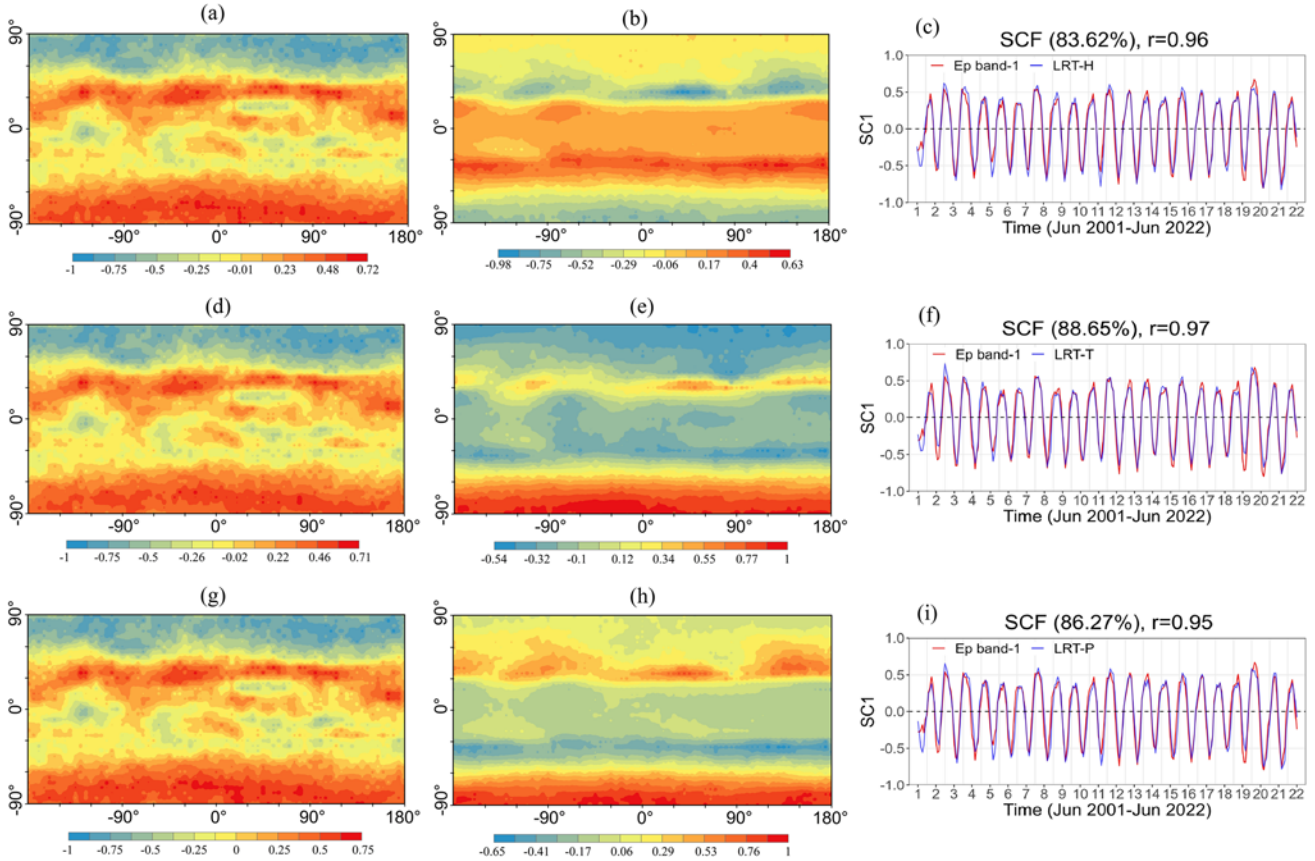

Fig. 8 The first leading mode of covariability for the coupled fields of Ep in height Band 1 and LRT parameters. Ep and LRT-H (**a**, **b**, **c**), Ep and LRT-T (**d**, **e**, **f**), and Ep and LRT-P (**g**, **h**, **i**). The spatial patterns for the first paired mode of covariability (SVD1) of GW Ep (left), LRT parameters SVD1 (middle), and the time series of the expansion coefficients (SC1) for the paired mode of both GW Ep and LRT parameter (right)

patterns of the combined GW activity in height Band 1 and the LRT parameters are highly coupled around the tropical belt zone and in the polar area in both hemispheres.

As shown in Fig. 9, the SCF of the first leading mode for the coupled fields of GW Ep in height Band 2 against LRT-H, LRT-T, and LRT-P explains about 91.01%, 93.44%, and 92.75%, respectively, of the total covariability of both fields. As is clear, SC1 of Ep in Band 2 has a strong positive correlation with that of LRT-H, LRT-T, and LRT-P of 0.98, 0.96, and 0.98, respectively (Fig. 9c, f, i). Furthermore, the SC1 for the temporal variability paired mode of GW Ep and all LRT parameters is dominated by inter-annual oscillations. The first coupled mode of spatial variability, SVD1, shows that the GW Ep in Band 2 (Fig. 9a) is characterized by observed fluctuations bands at the TEL and in the polar zones of both hemispheres, accompanied by LRT-H (Fig. 9b) fluctuations of the opposite sign over the same regions. The SVD1 of GW activity in height Band 2 (Fig. 9d) and LRT-T (Fig. 9e) shows that the GW Ep is characterized by observed fluctuation bands of opposite signs around the tropical zone and in the two poles, which are accompanied by LRT-T fluctuations of the same sign over the same regions. In the case of SVD1 for the spatial variability paired mode of Ep (Fig. 9g) and LRT-P (Fig. 9h), both have observed anomalies that exhibit good consistency globally. The SVD analysis results demonstrate that the patterns of the combined Ep in height Band 2 and the LRT parameters are highly coupled.

The SCF of the first dominant mode for the coupled fields of GW Ep in height Band 3 against LRT-H, LRT-T, and LRT-P accounts for 61.5%, 71.33%, and 67.16%, respectively, of the total covariability of both fields (Fig. 10). As is clear, SC1 of Ep in height Band 3 has a positive correlation with that of LRT-H, LRT-T, and LRT-P of 0.86, 0.86, and 0.85, respectively (Fig. 10c, f, i). Moreover, the SC1 for the temporal variability-paired mode of GW Ep and all LRT parameters is dominated by inter-annual oscillations. The prevailing mode for the coupled fields of GW Ep in height Band 3 against LRT parameters (Fig. 10) demonstrates that the patterns of the combined Ep and the LRT parameters are coupled and have accordance at the tropic's boundaries in both hemispheres. GW Ep in Band 3 (Fig. 10a) is characterized by weak fluctuations bands at the TELs, accompanied

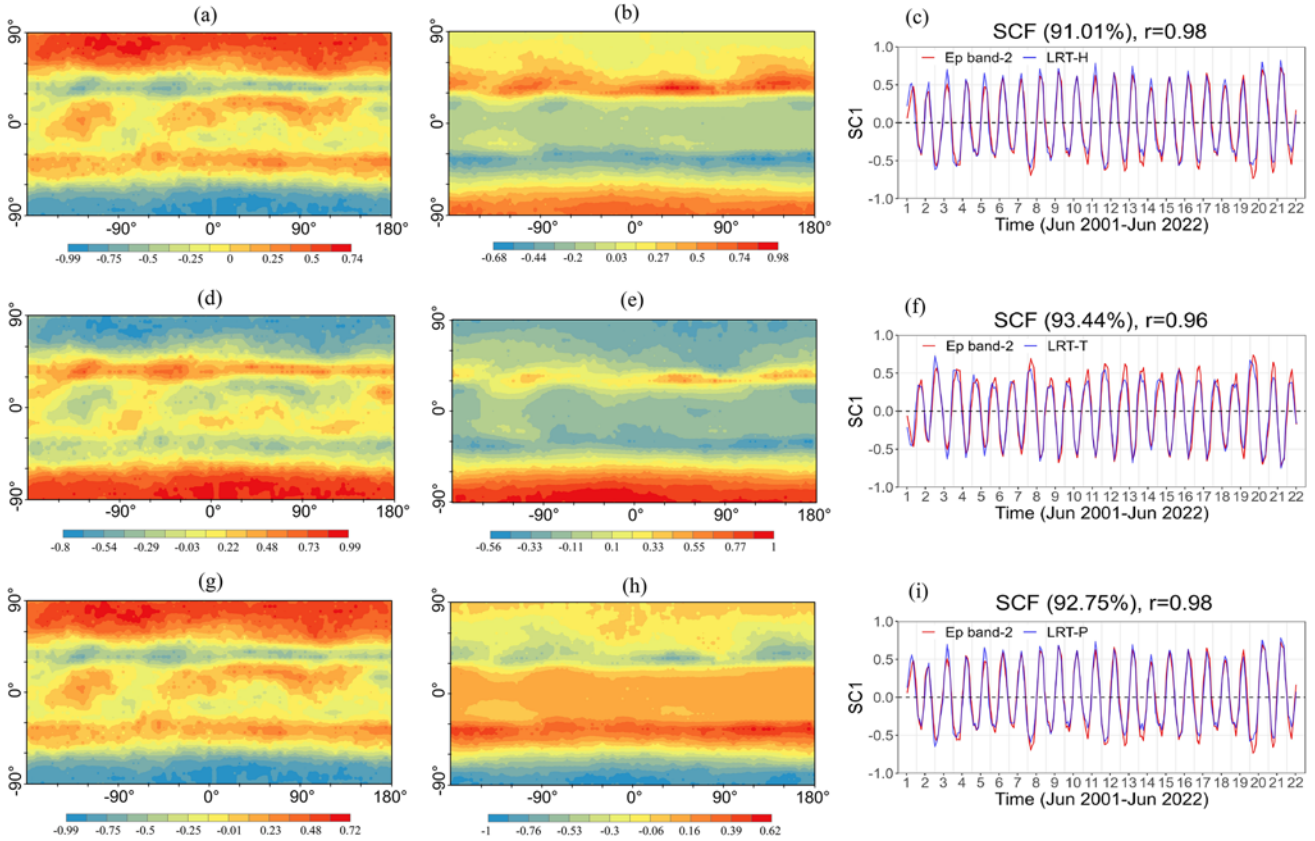

Fig. 9 The first leading mode of covariability for the coupled fields of Ep in height Band 2 and LRT parameters. Ep and LRT-H (**a**, **b**, **c**), Ep and LRT-T (**d**, **e**, **f**), and Ep and LRT-P (**g**, **h**, **i**). The spatial patterns for the first paired mode of covariability (SVD1) of GW Ep (left), LRT parameters SVD1 (middle), and the time series of the expansion coefficients (SC1) for the paired mode of both GW Ep and LRT parameter (right)

by LRT-H (Fig. 10b) wider fluctuations of the opposite sign over the same regions. The SVD1 of GW activity in height Band 3 (Fig. 10d) and LRT-T (Fig. 10e) depicts that the GW Ep is characterized by weak anomalies at the tropic's borders, which are accompanied by LRT-T fluctuations of the same sign over the same regions. In the case of SVD1, for the spatial variability paired mode of Ep (Fig. 10g) and LRT-P (Fig. 10h), both have fluctuations at the tropical boundaries of both hemispheres, but LRT-P has wider fluctuations than that of Ep. In height Band 3, the SVD analysis results demonstrate that the patterns of the combined Ep and the LRT parameters are less coupled in comparison to those in the case of height Bands 1 and 2.

3.3 Seasonal variation of GW Ep and LRT parameters

In this section, the seasonal variation of GW Ep at height Bands 1, 2, and 3 and that of LRT parameters are discussed. Global GW Ep has a clear seasonal variation. Figure 11a–d depicts the global spatial distribution of seasonal GW Ep variations at height Band 1 averaged from 2001 to 2022. The GW activity at height Band 1 demonstrates geographic changes with latitude from season to season. GW Ep values in height Band 1 range from 4.7 to 18.3 J/kg. As is clear in Fig. 11, GW activity shows two bands of high Ep values over the midlatitudes of both hemispheres; the high Ep bands in NH shifted poleward in JJA and SON (Fig. 11c, d). Over the south pole, the Ep values in DJF and MAM are higher than those in the north pole. In contrast, in JJA and SON, the Ep values at the north pole are higher than those at the south pole. As shown in Fig. 11e, all seasons have observed upward trends, and all seasons show significant variability over the period from 2001 to 2022. In addition, the GW activity in JJA and MAM is higher than that in DJF and SON. Figure 12 depicts the GW Ep seasonal variation in height Band 2, which represents the lower stratosphere. GW Ep values in height Band 2 range from 2.4 to 16.7 J/kg. It is clear that GW activity is high around the equator in all

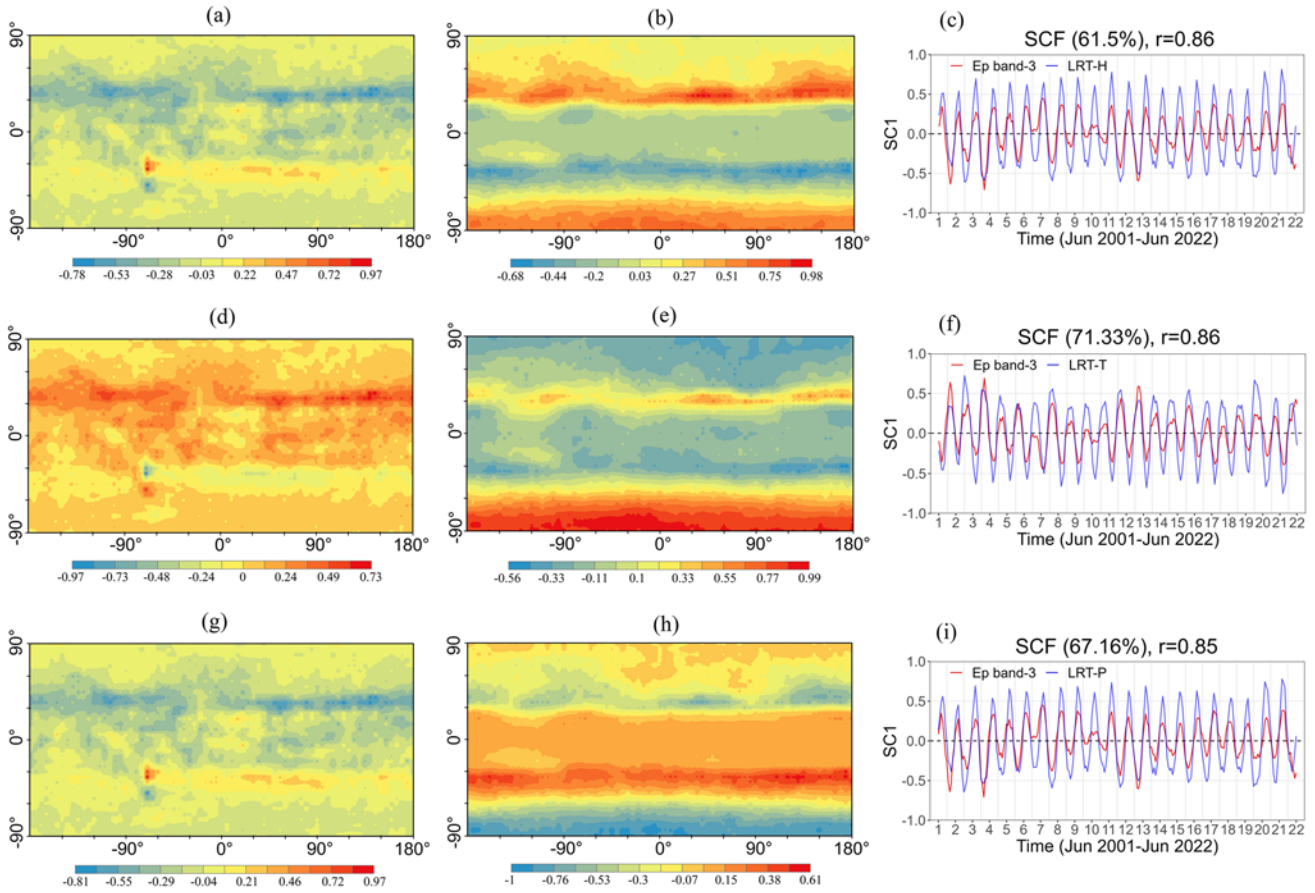

Fig. 10 The first leading mode of covariability for the coupled fields of Ep in height Band 3 and LRT parameters. Ep and LRT-H (**a**, **b**, **c**), Ep and LRT-T (**d**, **e**, **f**), and Ep and LRT-P (**g**, **h**, **i**). The spatial patterns for the first paired mode of covariability (SVD1) of GW Ep (left), LRT parameters SVD1 (middle), and the time series of the expansion coefficients (SC1) for the paired mode of both GW Ep and LRT parameter (right)

seasons (Fig. 12a–d). This zone of high Ep is followed by bands of low Ep poleward in both hemispheres. In DJF and MAM, the SH polar zone has high Ep values, while that of the NH polar zone is low. On the other hand, in JJA and SON, the NH polar zone has high GW Ep, while that of the SH exhibits low GW activity. All seasons have increasing Ep trends and significant variability over the period from 2001 to 2022 (Fig. 12e). In addition, the GW activity in MAM and DJF is higher than that in JJA and SON. The seasonality of GW Ep in height Band 3 is shown in Fig. 13. The Ep values in height Band 3 vary from 0.7 to 9.7 J/kg. The spatial pattern of GW activity in all seasons is quite similar, as the Ep values are high over the tropical belt and decrease poleward in both hemispheres. In DJF and MAM, the area of high GW Ep is located more toward the north pole, while in JJA and SON, it shows a shift toward the south pole. In the case of height Band 3, all seasons have downward Ep trends and significant variability over the period from 2001 to 2022 (Fig. 13e). In addition, the GW activity in DJF and MAM is higher than that in SON and JJA.

Figures 14, 15, and 16 depict the seasonal variation of LRT-H, LRT-T, and LRT-P, respectively, over the period from June 2001 to June 2022. The LRT-H (Fig. 14a–d) is maximum over the tropics at 17 km and minimum at the poles around 7 km. In all seasons, the area covered by high tropopause in NH is wider than that in SH. In the SH, the LRT-H is bimodally distributed spatially in mid- and high-latitude regions in JJA and SON (Fig. 14c, d). The seasonal variation of LRT-H is evident in polar locations, reflecting the impact of the polar general circulation (Liu et al. 2014). The spatial

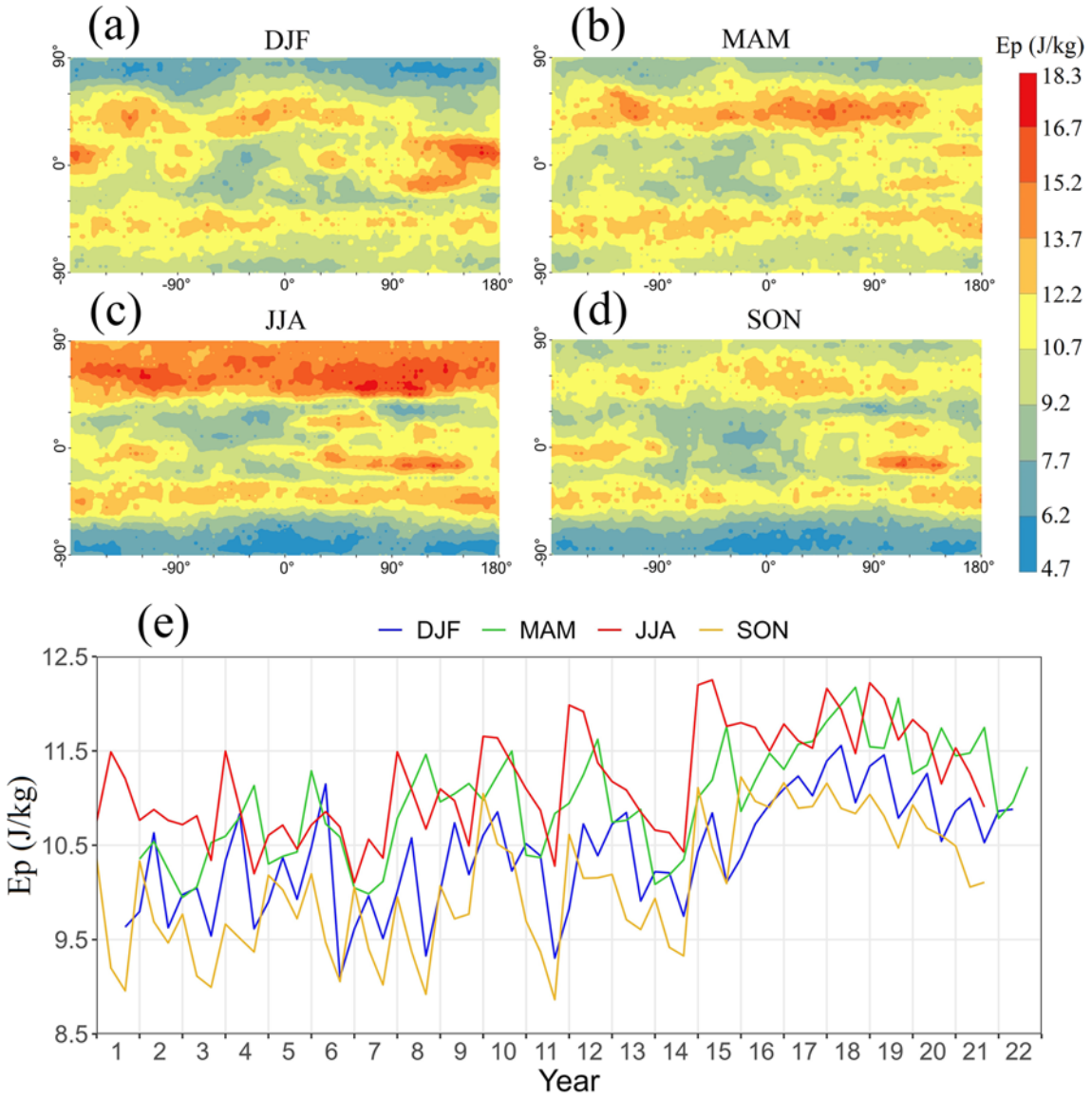

Fig. 11 Global spatial distribution of seasonal GW Ep variations at height Band 1 averaged from 2001 to 2022 (**a–d**) and time series for GW Ep at height Band 1 of all seasons from 2001 to 2022 (**e**)

pattern of seasonally averaged LRT-H around the equator shows agreement with that of GW Ep at height Bands 2 and 3 (Figs. 12 and 13). The LRT-H has increasing trends in all seasons (Fig. 14e). JJA has the maximum LRT-H upward trend, while MAM has the minimum LRT-H upward trend. Furthermore, the LRT-H values in JJA and SON are higher than those in DJF and MAM. The spatial pattern of seasonally averaged LRT-T (Fig. 15a–d) is minimum at the tropics around 188 K and maximum at mid- and high-latitudes around 227 K. In all seasons, LRT-T exhibits a clear bimodal pattern in the SH. The spatial pattern of LRT-T over the high latitudes of both hemispheres widely agrees with that of GW Ep at height Band 2 (Fig. 12). The spatial pattern of seasonally averaged LRT-P (Fig. 16a–d) is minimum at the tropics around 90 hPa and maximum at mid- and high latitudes around 360 hPa. The seasonal spatial pattern of LRT-P agrees with that of LRT-T but is opposite that of LRT-H. The spatial pattern of LRT-P over the high latitudes of both hemispheres is widely consistent

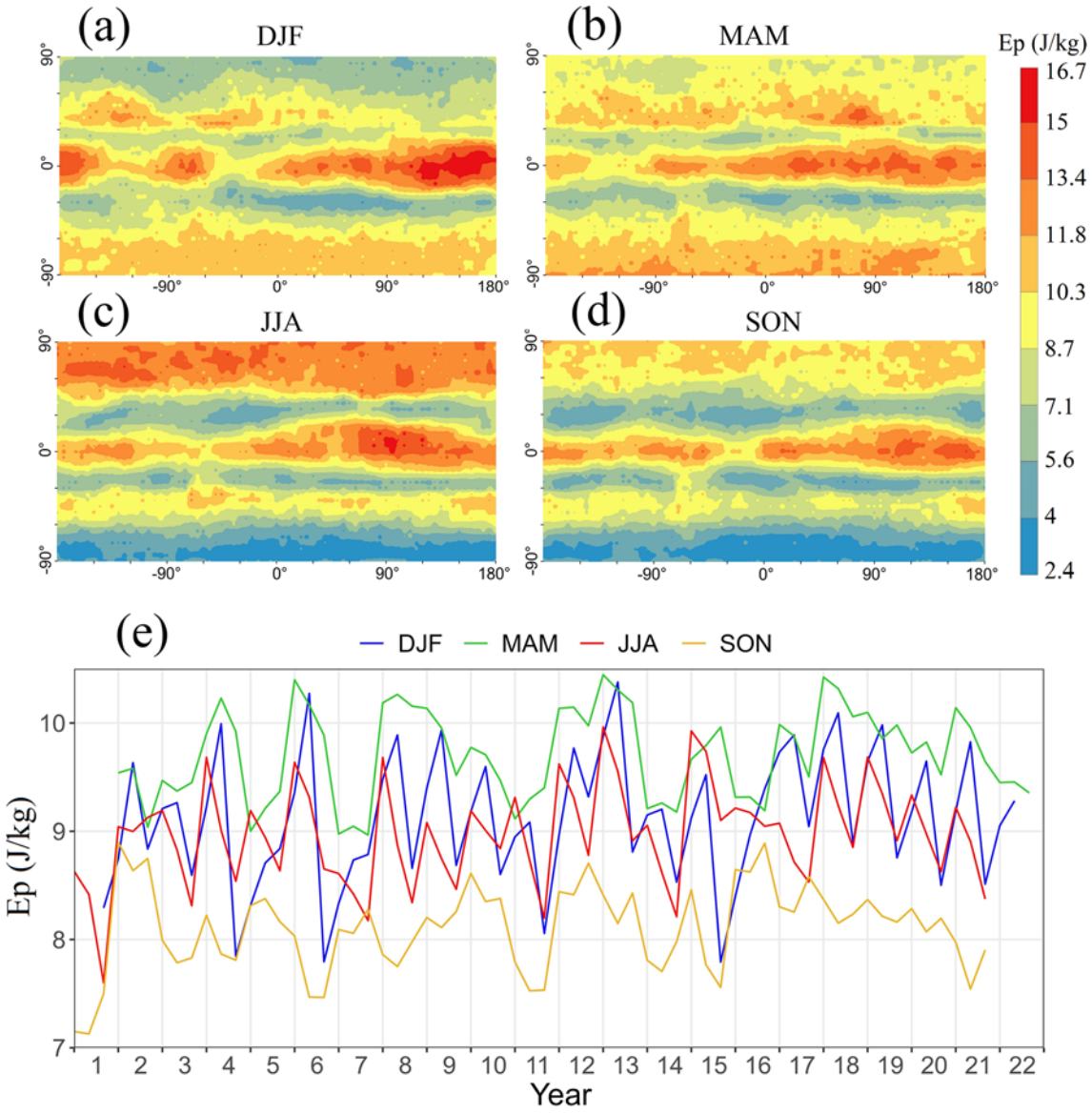

Fig. 12 Global spatial distribution of seasonal GW Ep variations at height Band 2 averaged from 2001 to 2022 (**a–d**) and time series for GW Ep at height Band 2 of all seasons from 2001 to 2022 (**e**)

with that of GW Ep at height Band 2 (Fig. 12). The LRT-P has decreasing trends in all seasons (Fig. 16e). JJA has the maximum LRT-P downward trend, while MAM has the minimum LRT-P downward trend. The seasonal trends of LRT-P (Fig. 16e) inversely agree with those of LRT-H (Fig. 14e). The values of LRT-T (Fig. 15e) and LRT-P (Fig. 16e) in DJF and MAM are higher than those of JJA and SON, showing consistency with the GW Ep at height Band 2. The results of LRT parameter seasonal patterns are in line with those of Son et al. (2011) and Liu et al. (2014).

4 Conclusions

The GNSS-RO is an exceptional atmospheric sounding technique for deriving atmospheric temperature structures. In this study, the relationship between GW activity, in terms

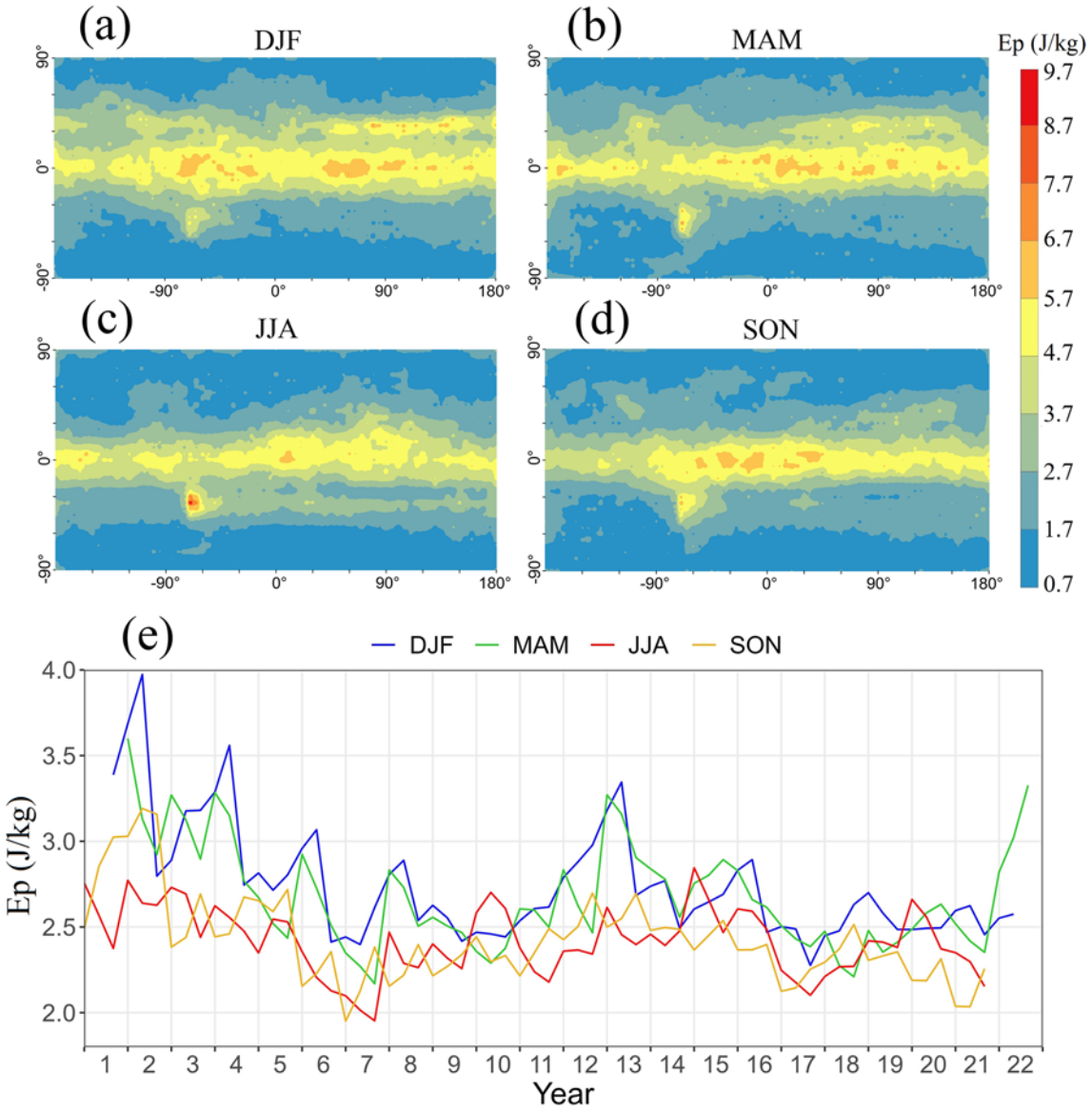

Fig. 13 Global spatial distribution of seasonal GW Ep variations at height Band 3 averaged from 2001 to 2022 (**a–d**) and time series for GW Ep at height Band 3 of all seasons from 2001 to 2022 (**e**)

of Ep, and the LRT parameters is widely investigated for the first time using data from 12 GNSS-RO missions for the period June 2001 to June 2022. Many studies have reported that the tropopause parameters are important in climate change research because their variability is highly related to the phenomenon of global warming (Sausen and Santer 2003; Seidel and Randel 2006; Mohd Zali and Mandeep 2019). Our study results indicate that the global LRT-H has increased by about 30 m/decade, and the LRT-T has an upward trend of 0.13 k/decade. On the other hand, LRT-P has a downward trend of − 0.76 hPa/decade.

The GW activity, in terms of Ep, is maximum in height Band 1 with an upward trend of about 0.62 J/kg per decade. In addition, in height Band 2, the GW Ep shows an increasing trend of about 0.18 J/kg per decade. In the case of height Band 3, the GW Ep is minimum with a downward trend of about − 0.17 J/kg per decade. The high GW Ep in Band 1 is attributed to the fact that most of the GW-generating

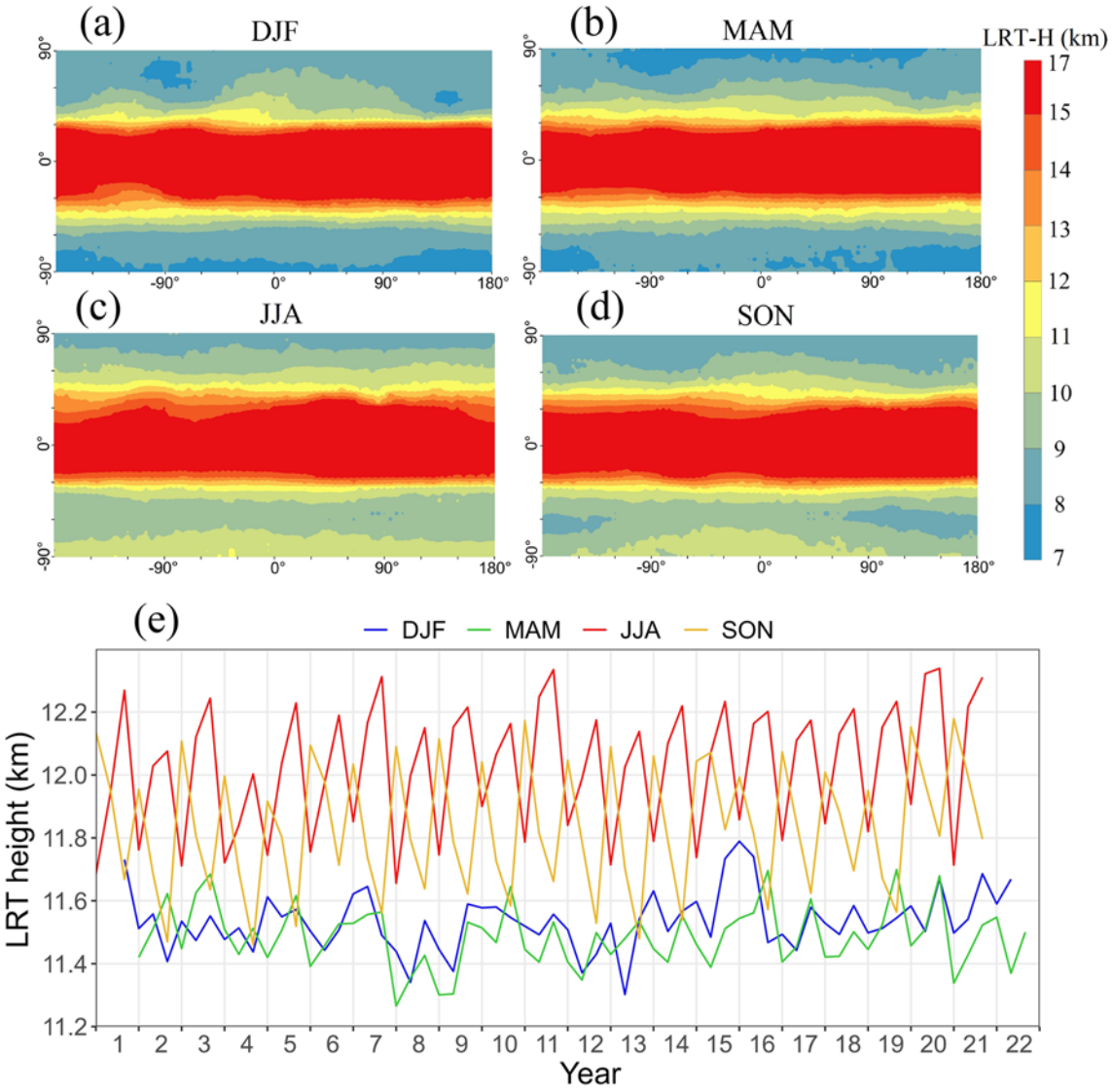

Fig. 14 Global spatial distribution of seasonal LRT-H variations averaged from 2001 to 2022 (**a–d**) and time series for LRT-H of all seasons from 2001 to 2022 (**e**)

sources are located in the troposphere. In height Band 2, the GW Ep has the strongest correlation coefficients with the LRT parameters (H, T, and P), which are about − 0.52, 0.76, and 0.6, respectively. Under the LRT level, the GW Ep increases over the period June 2001 to June 2022, which may indicate an increase in the atmosphere's instability and turbulence caused by changes in the activity of one or more GW-generating sources. The increase of GW activity under the LRT level matches that of LRT-H; thus, our results support those of Yu et al. (2019), who indicated that, at mid- and high-latitudes, LRT was lifted and became cooler when the atmospheric GWs propagated through the tropopause from the troposphere to the stratosphere.

The spatial–temporal analysis of LRT parameters and GW activity at all height bands, applying EOF, shows that there are significant positive correlation coefficients among PC1 of all LRT parameters and that of GW Ep at all height levels. The results of the EOF (PCA) analysis clarify the close effect of GW activity on tropopause parameters. The first leading mode of spatial variability, EOF1, of GW Ep has different spatial patterns upward from height Bands 1–3. On the relation

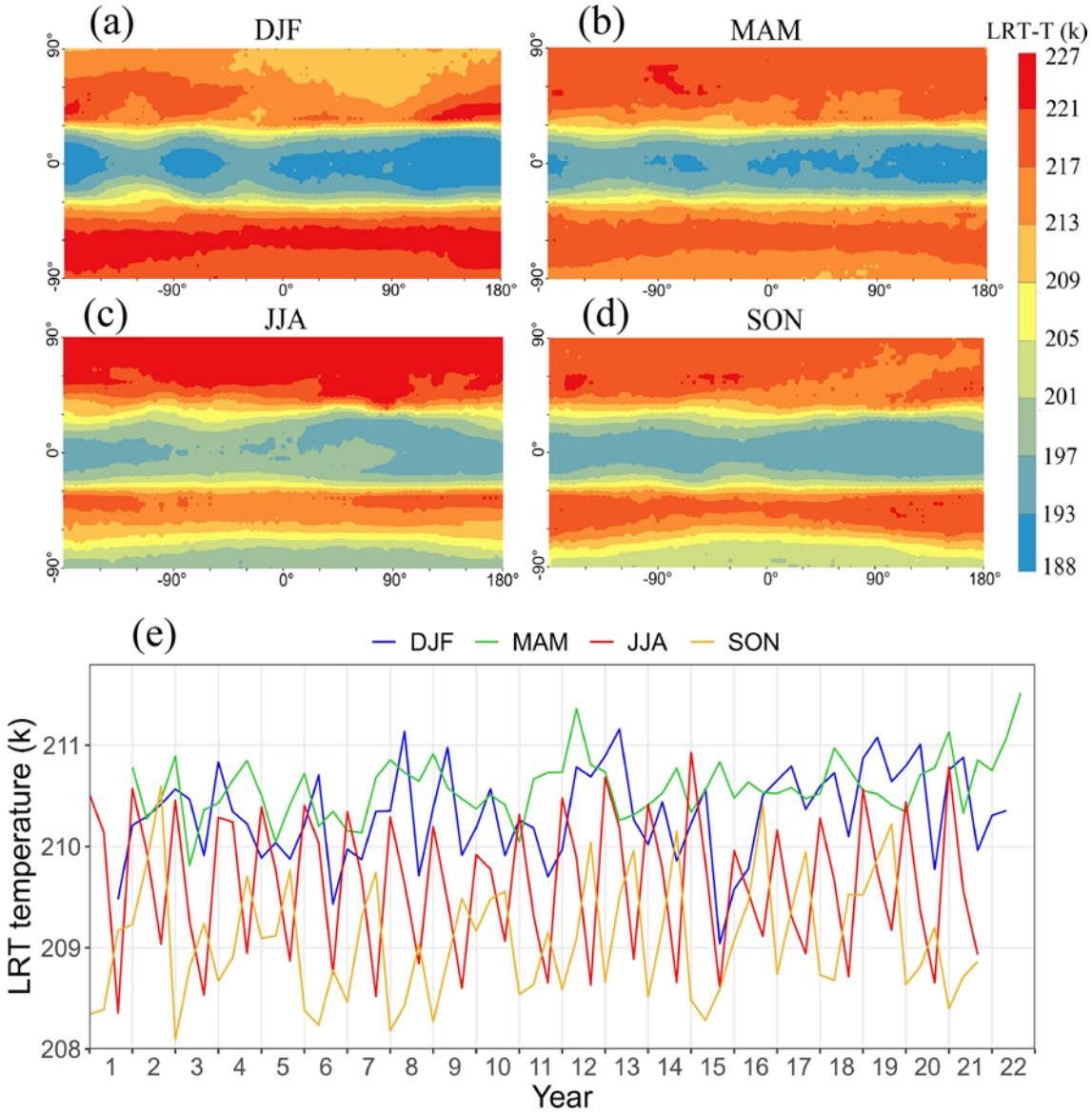

Fig. 15 Global spatial distribution of seasonal LRT-T variations averaged from 2001 to 2022 (**a–d**) and time series for LRT-T of all seasons from 2001 to 2022 (**e**)

between EOF1 of LRT parameters and that of GW Ep at different levels, the EOF1 of Ep in Band 2 agrees with that of LRT parameters, with variability modes of the same sign for both LRT-T and LRT-P and of the opposite sign in the case of the LRT-H. The WTC analysis between the leading mode (PC1) of GW Ep at all height bands and that of LRT parameters clarifies that the GW Ep and LRT parameters are in phase. GW activity at Band 1 and Band 2 has a high level of correlation with LRT parameters at different time scales along the study period. LRT-T has the highest coherence with GW Ep, especially at height Band 2. The results of the SVD analysis depict that for the GW Ep at all levels, the SC1 for the temporal variability paired mode of Ep and all LRT parameters is dominated by inter-annual oscillations. In addition, SC1 of Ep at all height bands has a significant positive correlation with that of LRT parameters. Moreover, the first coupled mode of spatial variability,

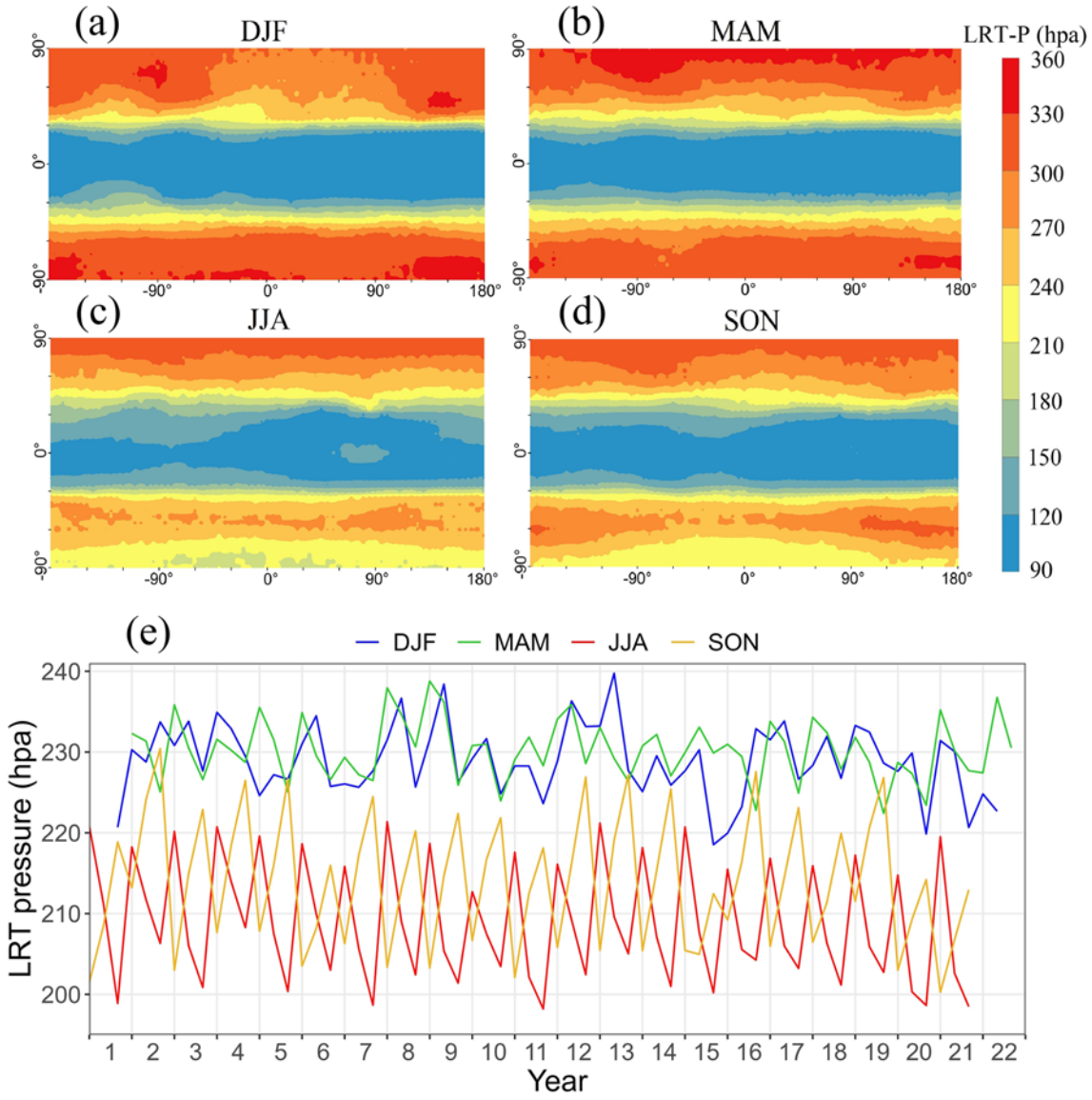

Fig. 16 Global spatial distribution of seasonal LRT-P variations averaged from 2001 to 2022 (**a–d**) and time series for LRT-P of all seasons from 2001 to 2022 (**e**)

SVD1, demonstrates that the GW Ep at Band 2 is characterized by observed fluctuations that are accompanied by observed fluctuations of the same sign in the cases of LRT-T and LRT-P and fluctuations of the opposite sign in the case of LRT-H. The SVD analysis results indicate that the pattern of the combined Ep and LRT parameters is highly coupled in height Band 2. Both global GW Ep and LRT parameters have a clear seasonal variation. The LRT parameters have seasonal pattern that is consistent with that of GW Ep at height Band 2. All analysis results affirm that the variability, coherence, and covariability of LRT parameters are connected and related to GW activity in height Band 2 (lower stratosphere) more than Band 1 and Band 3. In conclusion, the interaction between global GW activity and tropopause characteristics is clearly evident.

Acknowledgements The authors are thankful to the CDAAC for providing GNSS-RO data. In addition, the authors are grateful to Prof. Hatem Odah for his support. The first author expresses his gratitude to Egypt's National Research Institute of Astronomy and Geophysics and China's Nanjing University of Information Science and Technology for providing him with a scholarship to pursue his Ph.D.

Author contribution Conceptualization, M.D. and S.J.; methodology, M.D. and S.J.; software, M.D. and A.S.; validation, S.J. and M.D.;

formal analysis, M.D. and A.S.; investigation, S.J. and M.D.; resources, M.D.; data curation, M.D. and A.S.; writing—original draft preparation, S.J. and M.D.; writing—review and editing, S.J., M.D. and A.S.; visualization, M.D.; supervision, S.J.; project administration, S.J.; funding acquisition, S.J. All authors have read and agreed to the published version of the manuscript.

Funding This study was supported by the National Natural Science Foundation of China (NSFC) Project (Grant No. 12073012), China Scholarship Council (CSC), and Ministry of Higher Education of the Arab Republic of Egypt.

Data availability GNSS-RO data used in this paper are available at CDAAC archive (https://cdaac-www.cosmic.ucar.edu/, CDAAC 2022).

Declarations

Competing interests The authors declare no competing interests.

References

Alexander P, De La Torre A, Llamedo P et al (2011) A method to improve the determination of wave perturbations close to the tropopause by using a digital filter. Atmos Meas Tech 4:1777–1784. https://doi.org/10.5194/amt-4-1777-2011

Ayorinde TT, Wrasse CM, Barros S, et al (2022) The relationship between stratospheric gravity wave potential energy and tropospheric parameters over South America inferred from COSMIC-2 and METOP radio occultation measurements. https://doi.org/10.21203/rs.3.rs-2326789/v1

Bai W, Deng N, Sun Y, et al (2020) Applications of GNSS-RO to numerical weather prediction and tropical cyclone forecast. Atmosphere (Basel) 11. https://doi.org/10.3390/atmos11111204

Beyerle G, Heise S, Kaschenz J, Gert K (2006) Atmosphere and climate. Atmos Clim. https://doi.org/10.1007/3-540-34121-8

Birner T, Sankey D, Shepherd TG (2006) The tropopause inversion layer in models and analyses. Geophys Res Lett 33:13–16. https://doi.org/10.1029/2006GL026549

Bjornsson H, Venegas SA (1997) Manual for EOF and SVD analyses of climatic data. Center for Climate and Global Change Research. McGill University, CCGCR Report No. 97–1, Montréal, Québec, 52pp

Bretherton CS, Smith C, Wallace JM (1992) An intercomparison of methods for finding coupled patterns in climate data. 5:541–560

Calabia A, Jin S (2020) New modes and mechanisms of long-term ionospheric TEC variations from global ionosphere maps. J Geophys Res Sp Phys 125:1–16. https://doi.org/10.1029/2019JA027703

CDAAC (2022) COSMIC data analysis and archive center. https://cdaac-www.cosmic.ucar.edu/. [last access: 17 November 2022]

Corrigan CE, Ramanathan V, Schauer JJ (2006) Impact of monsoon transitions on the physical and optical properties of aerosols. J Geophys Res Atmos 111:1–15. https://doi.org/10.1029/2005JD006370

Cucurull L (2010) Improvement in the use of an operational constellation of GPS radio occultation receivers in weather forecasting. Weather Forecast 25:749–767. https://doi.org/10.1175/2009WAF2222302.1

Darrag M, Jin S, Calabia A, Samy A (2022) Determination of tropical belt widening using multiple GNSS radio occultation measurements. Ann Geophys 40:359–377. https://doi.org/10.5194/ANGEO-40-359-2022

Dubache G, Ogwang BA, Ongoma V, Towfiqul Islam ARM (2019) The effect of Indian Ocean on Ethiopian seasonal rainfall. Meteorol Atmos Phys 131:1753–1761. https://doi.org/10.1007/s00703-019-00667-8

Foelsche U, Borsche M, Steiner AK et al (2008) Observing upper troposphere-lower stratosphere climate with radio occultation data from the CHAMP satellite. Clim Dyn 31:49–65. https://doi.org/10.1007/s00382-007-0337-7

Forootan E, Awange JL, Kusche J et al (2012) Independent patterns of water mass anomalies over Australia from satellite data and models. Remote Sens Environ 124:427–443. https://doi.org/10.1016/j.rse.2012.05.023

Fritts DC, Alexander MJ (2003) Gravity wave dynamics and effects in the middle atmosphere. Rev Geophys 41:1–64. https://doi.org/10.1029/2001RG000106

Fritts DC, Nastrom GD (1992) Sources of mesoscale variability of gravity waves. Part II: frontal, convective, and jet stream excitation. J Atmos Sci 49:111–127

Grinsted A, Moore JC, Jevrejeva S (2004) Application of the cross wavelet transform and wavelet coherence to geophysical time series. Nonlinear Process Geophys 11(5/6):561–566. https://doi.org/10.5194/npg-11-561-2004

Hindley NP, Wright CJ, Smith ND, Mitchell NJ (2015) The southern stratospheric gravity wave hot spot: individual waves and their momentum fluxes measured by COSMIC GPS-RO. Atmos Chem Phys 15:7797–7818. https://doi.org/10.5194/acp-15-7797-2015

Ho SP, Hunt D, Steiner AK et al (2012) Reproducibility of GPS radio occultation data for climate monitoring: Profileto-profile intercomparison of CHAMP climate records 2002 to 2008 from six data centers. J Geophys Res Atmos 117:1–38. https://doi.org/10.1029/2012JD017665

Ho SP, Anthes RA, Ao CO et al (2020) The COSMIC/FORMOSAT-3 radio occultation mission after 12 years. Bull Am Meteorol Soc 101:E1107–E1136

Jin S (Ed) (2012) Global navigation satellite systems: signal, theory and applications. InTech-Publisher, Rijeka, p 426

Jin S, Gao C, Li J (2019) Atmospheric sounding from fengyun-3C GPS radio occultation observations: first results and validation. Adv Meteorol 2019:4780143. https://doi.org/10.1155/2019/4780143

Jin S, Cardellach E, Xie F (2014) GNSS remote sensing. Volume 19 of Remote Sensing and Digital Image Processing. Dordrecht: Springer. ISBN: 978–94–007–7482–7

Jin S, Han L, Cho J (2011) Lower atmospheric anomalies following the 2008 Wenchuan earthquake observed by GPS measurements. J Atmos Sol-Terr Phys 73(7–8):810–814. https://doi.org/10.1016/j.jastp.2011.01.023

Jin S, Jin R, Kutoglu H (2017) Positive and negative ionospheric responses to the March 2015 geomagnetic storm from BDS observations. J Geod 91:613–626. https://doi.org/10.1007/s00190-016-0988-4

Khan A, Jin S (2016) Effect of gravity waves on the tropopause temperature, height and water vapor in Tibet from COSMIC GPS radio occultation observations. J Atmos Solar-Terrestrial Phys 138–139:23–31. https://doi.org/10.1016/j.jastp.2015.12.001

Kumar V, Dhaka SK, Reddy KK et al (2014) Impact of quasi-biennial oscillation on the inter-annual variability of the tropopause height and temperature in the tropics: a study using COSMIC/FORMOSAT-3 observations. Atmos Res 139:62–70. https://doi.org/10.1016/j.atmosres.2013.12.014

Kunkel D, Hoor P, Wirth V (2014) Can inertia-gravity waves persistently alter the tropopause inversion layer? Geophys Res Lett 41:7822–7829. https://doi.org/10.1002/2014GL061970

Kursinski ER, Hajj GA, Schofield JT et al (1997) Observing Earth's atmosphere with radio occultation measurements using the global positioning system. J Geophys Res Atmos 102:23429–23465. https://doi.org/10.1029/97jd01569

Li W, Yuan Y-b, Chai YJ et al (2017) Characteristics of the global thermal tropopause derived from multiple radio occultation

measurements. Atmos Res 185:142–15. https://doi.org/10.1016/j.atmosres.2016.09.013
Liu Y, Xu T, Liu J (2014) Characteristics of the seasonal variation of the global tropopause revealed by COSMIC/GPS data. Adv Sp Res 54:2274–2285. https://doi.org/10.1016/j.asr.2014.08.020
Mchugh J, Sharman R (2013) Generation of mountain wave-induced mean flows and turbulence near the tropopause. Q J R Meteorol Soc 139:1632–1642. https://doi.org/10.1002/qj.2035
Meng L, Liu J, Tarasick DW et al (2021) Continuous rise of the tropopause in the Northern Hemisphere over 1980–2020. Sci Adv 7:1–10. https://doi.org/10.1126/sciadv.abi8065
Miyazaki K, Sato K, Watanabe S et al (2010) Transport and mixing in the extratropical tropopause region in a high-vertical-resolution GCM. Part II: relative importance of large-scale and small-scale dynamics. J Atmos Sci 67:1315–1336. https://doi.org/10.1175/2009JAS3334.1
Mohd Zali R, Mandeep JS (2019) The tropopause height analysis in equatorial region through the GPS-RO. E3S Web Conf 76. https://doi.org/10.1051/e3sconf/20197604002
Namboothiri SP, Jiang JH, Kishore P et al (2008) CHAMP observations of global gravity wave fields in the troposphere and stratosphere. J Geophys Res Atmos 113:1–11. https://doi.org/10.1029/2007JD008912
Oscar (2023) https://www.wmo-sat.info/oscar/gapanalyses?mission=9. [last access: on 23 February]
Perrett JA, Wright CJ, Hindley NP et al (2021) Determining gravity wave sources and propagation in the Southern Hemisphere by ray-tracing AIRS measurements. Geophys Res Lett 48:1–10. https://doi.org/10.1029/2020GL088621
Pisoft P, Sacha P, Polvani LM, et al (2021) Stratospheric contraction caused by increasing greenhouse gases. Environ Res Lett 16. https://doi.org/10.1088/1748-9326/abfe2b
Randel WJ, Wu F, Rivera Ríos W (2003) Thermal variability of the tropical tropopause region derived from GPS/MET observations. J Geophys Res Atmos 108:1–12. https://doi.org/10.1029/2002jd002595
Ratnam MV, Tetzlaff G, Jacobi C (2004) Global and seasonal variations of stratospheric gravity wave activity deduced from the CHAMP/GPS satellite. J Atmos Sci 61:1610–1620. https://doi.org/10.1175/1520-0469(2004)061%3c1610:GASVOS%3e2.0.CO;2
Santer BD, Wigley TML, Simmons AJ et al (2004) Identification of anthropogenic climate change using a second-generation reanalysis. J Geophys Res D Atmos 109:1–19. https://doi.org/10.1029/2004JD005075
Satheesan K, Krishna Murthy BV (2005) Modulation of tropical tropopause by wave disturbances. J Atmos Solar-Terrestrial Phys 67:878–883. https://doi.org/10.1016/j.jastp.2005.02.011
Sausen R, Santer BD (2003) Use of changes in tropopause height to detect human influences on climate. Meteorol Zeitschrift 12:131–136. https://doi.org/10.1127/0941-2948/2003/0012-0131
Scherllin-Pirscher B, Steiner AK, Anthes RA et al (2021) Tropical temperature variability in the UTLS: new insights from GPS radio occultation observations. J Clim 34:2813–2838. https://doi.org/10.1175/JCLI-D-20-0385.1
Schmidt T, Alexander P, de la Torre A (2016) Stratospheric gravity wave momentum flux from radio occultations. J Geophys Res 121:4443–4467. https://doi.org/10.1002/2015JD024135
Schmidt T, Wickert J, Beyerle G, Heise S (2008) Global tropopause height trends estimated from GPS radio occultation data. Geophys Res Lett 35:1–5. https://doi.org/10.1029/2008GL034012
Schmidt T, Wickert J, Beyerle G, Reigber C (2004) Tropical tropopause parameters derived from GPS radio occultation measurements with CHAMP. J Geophys Res D Atmos 109:1–13. https://doi.org/10.1029/2004JD004566
Seidel DJ, Randel WJ (2006) Variability and trends in the global tropopause estimated from radiosonde data. J Geophys Res Atmos 111:1–17. https://doi.org/10.1029/2006JD007363
Sharman RD, Trier SB, Lane TP, Doyle JD (2012) Sources and dynamics of turbulence in the upper troposphere and lower stratosphere: a review. Geophys Res Lett 39:1–9. https://doi.org/10.1029/2012GL051996
Son SW, Tandon NF, Polvani LM (2011) The fine-scale structure of the global tropopause derived from COSMIC GPS radio occultation measurements. J Geophys Res Atmos 116:1–17. https://doi.org/10.1029/2011JD016030
Steiner AK, Lackner BC, Ladstdter F et al (2011) GPS radio occultation for climate monitoring and change detection. Radio Sci 46:1–17. https://doi.org/10.1029/2010RS004614
Tegtmeier S, Anstey J, Davis S et al (2020) Temperature and tropopause characteristics from reanalyses data in the tropical tropopause layer. Atmos Chem Phys 20:753–770. https://doi.org/10.5194/acp-20-753-2020
Tsuda T, Nishida M, Rocken C, Ware RH (2000) A global morphology of gravity wave activity in the stratosphere revealed by the GPS occultation data temperature perturbations with vertical wavelengths ranging from 2 to 10 km and we have then derived the global distribution than over the Pacific Ocean. Science (80-) 105:7257–7273
Wang L, Alexander MJ (2010) Global estimates of gravity wave parameters from GPS radio occultation temperature data. J Geophys Res Atmos 115:1–12. https://doi.org/10.1029/2010JD013860
WMO (1957) Meteorology a three-dimensional science: second session of the commission for aerology, WMO Bulletin IV (4). WMO, Geneva, pp 134–138
Xu X, Gao P, Zhang X (2014) Global multiple tropopause features derived from COSMIC radio occultation data during 2007 to 2012. 119:8515–8534. https://doi.org/10.1002/2014jd021620
Yang SS, Pan CJ, Das U (2021) Investigating the spatio-temporal distribution of gravity wave potential energy over the equatorial region using the era5 reanalysis data. Atmosphere (Basel) 12. https://doi.org/10.3390/atmos12030311
Yu D, Xu X, Luo J, Li J (2019) On the relationship between gravity waves and tropopause height and temperature over the globe revealed by COSMIC radio occultation measurements. Atmosphere (Basel) 10:1–15. https://doi.org/10.3390/atmos10020075
Zängl G, Hoinka KP (2001) The tropopause in the polar regions. J Clim 14:3117–3139. https://doi.org/10.1175/1520-0442(2001)014%3c3117:TTITPR%3e2.0.CO;2
Zeng Z, Sokolovskiy S, Schreiner WS, Hunt D (2019) Representation of vertical atmospheric structures by radio occultation observations in the upper troposphere and lower stratosphere: comparison to high-resolution radiosonde profiles. J Atmos Ocean Technol 36:655–670. https://doi.org/10.1175/JTECH-D-18-0105.1
Zhang SD, Yi F, Huang CM, Huang KM (2012) High vertical resolution analyses of gravity waves and turbulence at a midlatitude station. J Geophys Res Atmos 117:1–15. https://doi.org/10.1029/2011JD016587
Zhang SD, Yi F, Huang CM, Zhou Q (2010) Latitudinal and seasonal variations of lower atmospheric inertial gravity wave energy revealed by US radiosonde data. Ann Geophys 28:1065–1074. https://doi.org/10.5194/angeo-28-1065-2010
Zhang Y, Zhang S, Huang C, Huang K, Gong Y, Gan Q (2015) The interaction between the tropopause inversion layer and the inertial gravity wave activities revealed by radiosonde observations at a midlatitude station. J Geophys Res Atmos 120:8099–8111. https://doi.org/10.1002/2015JD023115